Editors' Suggestion

Intrinsic and Extrinsic Factors Influencing the Dynamics of VO_2 Mott Oscillators

Stephanie M. Bohaichuk,[1,*] Suhas Kumar,[2,†] Mahnaz Islam,[1] Miguel Muñoz Rojo,[1,3]
R. Stanley Williams,[4] Gregory Pitner,[1] Jaewoo Jeong,[5] Mahesh G. Samant,[5] Stuart S.P. Parkin,[5]
and Eric Pop[1,6]

[1] *Department of Electrical Engineering, Stanford University, Stanford, California, USA*
[2] *Sandia National Laboratories, Livermore, California, USA*
[3] *Department of Thermal and Fluid Engineering, University of Twente, Enschede, Netherlands*
[4] *Department of Electrical & Computer Engineering, Texas A&M University, College Station, Texas, USA*
[5] *IBM Almaden Research Center, San Jose, California, USA*
[6] *Department of Materials Science and Engineering, Stanford University, Stanford, California, USA*

(Received 4 September 2022; accepted 30 January 2023; published 10 April 2023)

Oscillatory devices have recently attracted significant interest as key components of computing systems based on biomimetic neuronal spiking. An understanding of the time scales underlying the spiking is essential for engineering fast, controllable, low-energy devices. However, we find that the intrinsic dynamics of these devices is difficult to properly characterize, as they can be heavily influenced by the external circuitry used to measure them. Here we demonstrate these challenges using a VO_2 Mott oscillator with a sub-100-nm effective size, achieved using a nanogap cut in a metallic carbon nanotube electrode. Given the nanoscale thermal volume of this device, it would be expected to exhibit rapid oscillations. However, due to external parasitics present within commonly used current sources, we see orders-of-magnitude slower dynamics. We outline methods for determining when measurements are dominated by extrinsic factors and discuss the operating conditions under which intrinsic oscillation frequencies may be observed.

DOI: 10.1103/PhysRevApplied.19.044028

I. INTRODUCTION

Brain-inspired computing has attracted much interest as a path to more efficient artificial intelligence. Hardware implementations of such systems often require fast, controllable, low-energy sources of neuronlike spiking [1,2]. Such spiking can be produced in compact memristive switches, which are two-terminal devices exhibiting electronic instabilities like negative differential resistance (NDR), often constructed using channel-forming oxides [3], chalcogenides [4], or Mott insulators that undergo an insulator-metal transition (IMT) [5–7]. Examples of Mott insulators include vanadium dioxide (VO_2) and niobium dioxide (NbO_2), which undergo an IMT at around 340 K and 1070 K, respectively. As the temperature is increased above this IMT temperature, the material undergoes an abrupt increase in conductivity, typically by several orders of magnitude, which reverses upon cooling.

Devices constructed from such switching materials frequently exhibit strong coupling between nonlinear thermally-activated electrical transport and localized Joule heating [8,9]. When measured using a voltage source, feedback between these processes leads to abrupt volatile switching in current and resistance, but when a device is driven by a current source, it displays an electronic instability and NDR. When biased within the region of NDR in the presence of one or more parallel capacitors, the volatile resistive switching of the device, together with the parallel capacitor's charging and discharging, can produce periodic self-sustained oscillations in the device voltage and current. This setup is known as a relaxation oscillator or a Pearson-Anson oscillator, and can produce sharp spiking, useful in the construction of biomimetic circuits [10–16]. The parallel capacitor involved in excitations can originate from intrinsic device capacitance, unintended external parasitics, or intentionally added external capacitor(s). Identifying which of these capacitances are driving the dynamics and influencing the oscillation frequency can be challenging, especially because current source instabilities can complicate measurements of oscillations. Consequently, the resulting oscillation frequencies can be incorrectly assigned to the device's intrinsic thermal and electrical time scales.

In this work, we probe the IMT in sub-100-nm regions of VO_2 using a nanogap cut in a single-wall metallic carbon nanotube (CNT), which forms ultranarrow electrodes approximately 1 nm in diameter. This nanogap

*sbohaichuk@alumni.stanford.edu
†su1@alumni.stanford.edu

 © 2023 American Physical Society

test platform was inspired by previous work with phase-change memory [17], but has not been applied to volatile switches until now. We expect that an increase in oscillation frequency and reduction in energy might be gained by shrinking Mott switches down to the nanoscale, especially if device capacitance reduces [6,18]. However, despite the extremely small volume (low thermal mass) heated and cooled across the IMT, these nanogap devices oscillate at (kilohertz) frequencies comparable to much larger, micrometer-sized devices due to the influence of electrical capacitance from the current source. In contrast, we find that we are able to access intrinsic device dynamics in devices with a single metallic CNT used as an additional nanoscale heat source, either by reconnecting the cut CNT with metallic VO_2 at higher bias or by using a continuous CNT [19]. We address means for identifying the dominant electrical capacitance involved in oscillations as either intrinsic or extrinsic to the device. We also show that device dynamics may be effectively switched between different driving capacitors depending on the choice of the series resistor as well as electrothermal device parameters, providing a means to reconfigure spiking frequency and avoid current source interference.

II. RESULTS AND DISCUSSION

A. Nanogap device structure and characterization

As shown in Figs. 1(a) and 1(b), we fabricate nanoscale VO_2 devices by utilizing single-walled metallic CNTs approximately 1 nm in diameter as electrodes. Aligned CNTs are grown on a quartz substrate and transferred [21,22] onto a thin film (5 nm thick) of VO_2 grown epitaxially [23] on TiO_2 (101). After patterning the VO_2 by wet etching, 50-nm-thick Pd is deposited to make metallic contacts with both the VO_2 and CNTs [22]. A CNT running between the contacts is physically cut near its midpoint by using an atomic force microscope (AFM) tip (see Sec. 1 of the Supplemental Material [24] for additional fabrication details including lithography, etching, and AFM cutting).

The current-voltage behavior of the nanogap device [Fig. 1(c), corresponding to the device in Fig. 1(b)] at lower voltages (below 8 V) is dominated by the insulating VO_2 in the nanogap, with an IMT occurring in the gap at $V_S = 8.3$ V (abrupt jump in current marked “IMT1”). Once the VO_2 in the gap becomes metallic, as V_S is increased, the now metallically connected CNT acts as a localized Joule heater (i.e., the gap in the CNT is shorted by the metallic VO_2 within). This causes a second, larger IMT (marked “IMT2”) in the VO_2 along the length of the CNT, associated with a region of NDR (seen once the voltage drop across R_S is subtracted; see Supplemental Material Fig. S2 [24]) between $V_S = 20$ V and 23.4 V, followed by an abrupt jump in current at around 23.4 V. The IMT2 behavior is similar to that observed in previous work with a continuous (uncut) CNT as the heater [22]. Switching is repeatable and similar among other CNT-VO_2 nanogap devices, although the switching voltage and magnitude of change in resistance are dependent on the nanogap length (see Secs. 2 and 4 of the Supplemental Material [24]).

To experimentally validate the nanoscale heated volume and switching region associated with each IMT in these devices, we use Kelvin probe microscopy (KPM) and scanning thermal microscopy (SThM), two scanning probe techniques with sub-100-nm spatial resolution. KPM maps the local surface potential in a biased device, and when the image is first-order flattened (i.e., by removing the average

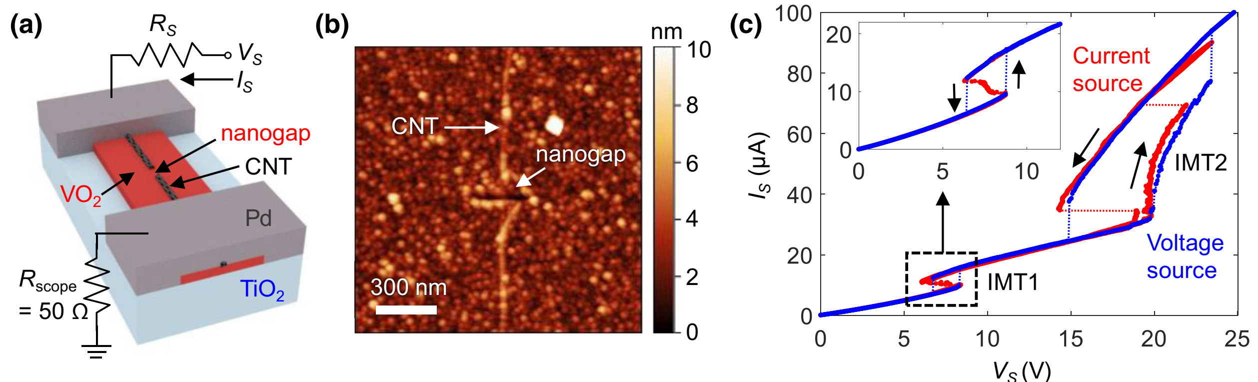

FIG. 1. CNT-VO_2 nanogap structure and static behavior. (a) Schematic illustration and measurement setup for a VO_2 device with a cut metallic CNT on top forming the electrodes. R_{scope} is the resistance of the measurement oscilloscope and $R_S = 200$ kΩ is a series resistor reducing current overshoot [20] and overheating failures. (b) AFM image of a CNT on VO_2 after cutting the CNT with an AFM tip, creating a nanogap of less than 100 nm. (c) Typical quasistatic current-voltage characteristics of a nanogap device measured using a voltage source (blue) and a current source (red), showing that switching occurs in two steps. The first corresponds to the IMT of the nano-sized VO_2 volume within the CNT gap (IMT1), and the second to the larger IMT volume of VO_2 between the Pd metal contacts along the CNT (IMT2), which is connected by metallic (post-IMT1) VO_2 within the nanogap. The inset magnifies IMT1 with identical units on the axes.

linear potential drop between metal contacts; see Sec. 3 of the Supplemental Material [24]), regions of contrast highlight changes in resistance and electric field [22,25]. KPM of a nanogap device held at $V_S = 8$ V, just prior to IMT1, exhibits sharp contrast at the CNT nanogap [Fig. 2(a)], indicating a concentrated field within it.

Additionally, we use SThM to map changes in device heating [22,26], as seen on the surface of a 35-nm poly(methyl methacrylate) (PMMA) capping layer used to electrically isolate the SThM tip from the device. The same device at an identical bias imaged using SThM exhibits localized heating within the nanogap [Fig. 2(b)], while no significant heating is observed along the rest of the CNT or VO_2. This is consistent with finite-element electrothermal simulations [Fig. 2(c)] based on a thermally induced IMT in the nanogap (see Sec. 4 of the Supplemental Material [24]), which shows that significant heating occurs only in the VO_2 within the gap and at the interface between the VO_2 and cut CNT ends. Heating at the two CNT tips forming the nanogap is dominant in the simulation, but blurring due to the finite tip size and thermal exchange radius [27] can cause the experimental appearance of a single hot spot centered on the gap. At a bias just beyond IMT1, the simulated maximum temperature of the VO_2 in the nanogap is only about 10 K above its IMT temperature ($T_{IMT} = 328$ K) in steady state.

Beyond IMT1 but prior to inducing IMT2 (at $V_S = 16$ V), much weaker contrast is observed in the flattened KPM image in Fig. 2(d), consistent with a lower voltage drop and field across the VO_2 in the gap, which turns metallic after IMT1. SThM [Fig. 2(e)] at this bias indicates that heating occurs not only in the gap, but also along the full length of the CNT, indicating that the CNT is effectively reconnected by the metallic VO_2 in the gap. Finite-element simulations shown in Fig. 2(f) also confirm

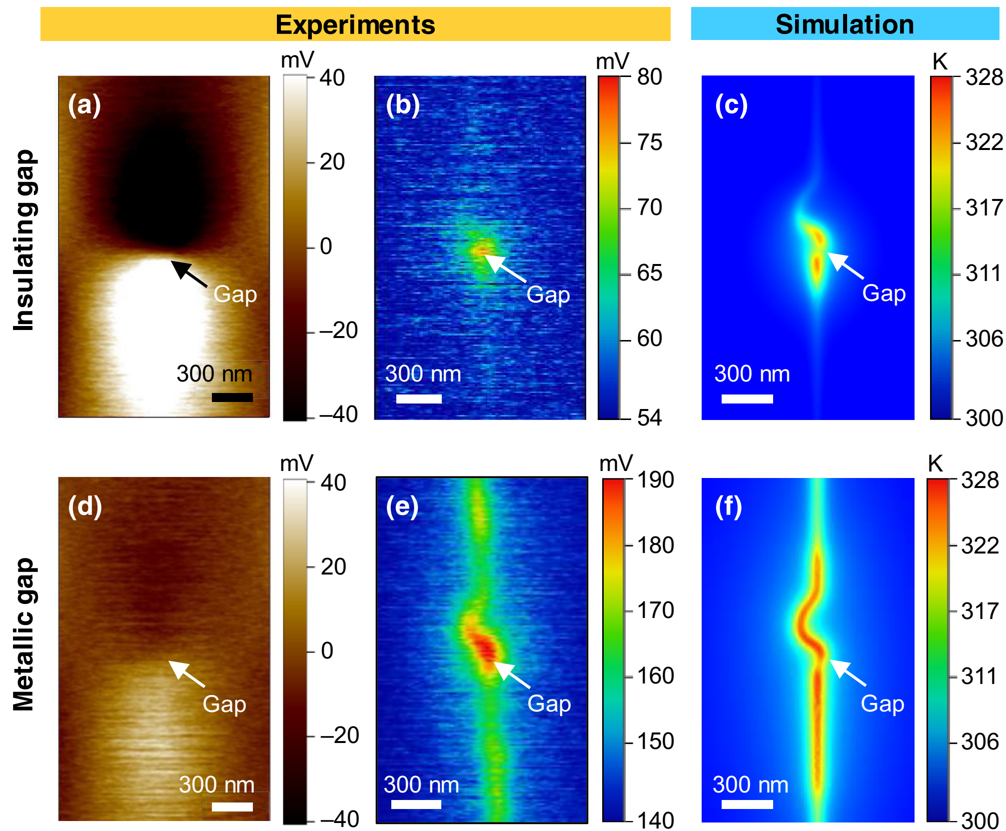

FIG. 2. Localized electric field and temperature during IMT1 and IMT2. (a) Flattened KPM image of a nanogap device held at $V_S = 8$ V (with $R_S = 200$ kΩ), just prior to IMT1. First-order flattening of the surface potential removes the average linear potential drop between the Pd contacts, and the contrast at the gap indicates a strong field within it [24]. The positive contact (ground) is outside the bottom (top) of each image. (b) SThM image of the same bias in the same device (now capped by PMMA) showing highly localized heating in the gap. The color bar refers to the SThM voltage, which is a measure of the change in local temperature on the PMMA surface. (c) Simulation of the capped nanogap device, showing the temperature on the PMMA surface prior to IMT1. (d) Flattened KPM image of the same device at $V_S = 16$ V, after IMT1 but before IMT2. There is a lower potential drop across the gap once it is metallic. (e) SThM image of the same bias and device (capped by PMMA), showing heating in the gap and also along the rest of the now-connected CNT. (f) Corresponding simulation of the capped device temperature on the PMMA surface, after IMT1.

heating of the VO_2 along the entire CNT length, leading to IMT2.

B. Origin of oscillation frequencies

When biased using a constant current within a region of NDR, it is possible to produce self-sustained periodic electrical oscillations, aided by an external or internal parallel capacitor [11,19,28]. In a comparable micrometer-scale VO_2 device made *without* a CNT ($L = 3.5$ μm, $W = 2.7$ μm) oscillations occur with a frequency of about 0.4 kHz [Fig. 3(a)], consisting of a fast initial spike of about 70 ns [inset of Fig. 3(d)] followed by a slow decay of 0.44 ms. Due to the reduced sampling rate of the oscilloscope at longer acquisition durations, the fast initial spike is not captured in Figs. 3(a) and 3(d) but is shown at shorter time scales in the inset to Fig. 3(d). In the nanogap device of Fig. 1, oscillations occur at IMT1 (corresponding to the nanogap volume) with a frequency of about 0.6 kHz [Fig. 3(b)]. A fast initial spike does not appear to be present, but only a slow decay of 1.2 ms after the IMT step. Thus, despite an enormous reduction in the volume of VO_2 heated and cooled across the IMT [observed in Figs. 2(a)–2(c)], the CNT nanogap device oscillates at nearly the same frequency as the large VO_2-only device. Similar slow oscillations are observed in other nanogap devices in IMT1 (see Sec. 2(b) of the Supplemental Material [24]).

In contrast, when the same CNT nanogap device is biased within IMT2, the CNT is reconnected as a Joule heating source (in series with the metallic VO_2 bridging the gap) and oscillations are observed to be over 1000 times faster with a frequency of 0.65 MHz [Figs. 3(c) and 3(f)]. This observation is surprising if oscillations are set solely by intrinsic electrical and thermal time constants because the volume for the IMT2 "connected nanogap" is much larger than for the IMT1 nanogap (evidenced by Fig. 2), and a larger volume usually implies slower dynamics. Yet, the IMT2 connected nanogap appears orders of magnitude

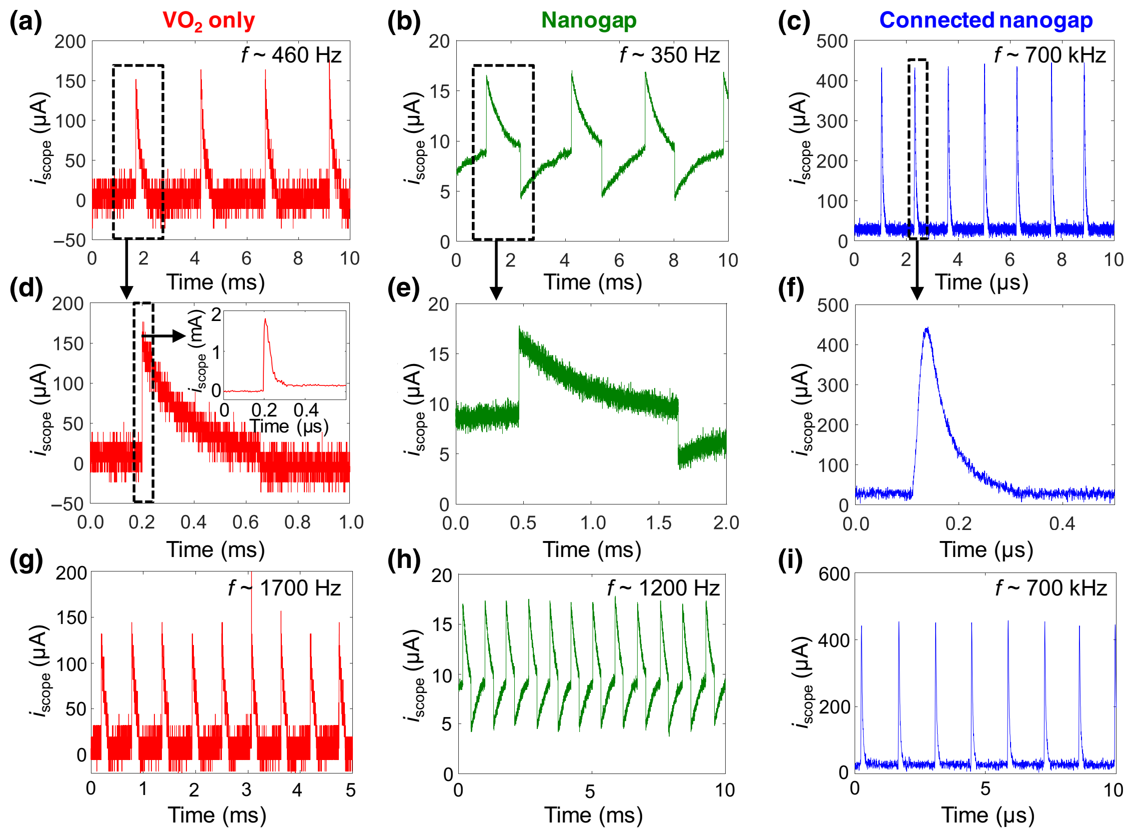

FIG. 3. Dynamics in VO_2 devices with and without a nanogap. Oscillations are measured with a 50 Ω oscilloscope in series, when the device is biased with a constant current in a region of negative differential resistance (NDR). (a) A micrometer-scale VO_2 device ($L = 3.5$ μm, $W = 2.7$ μm) without a CNT, corresponding to oscillations of a large volume of VO_2. (b) A CNT nanogap device biased in IMT1, corresponding to oscillations of a nanoscale volume of VO_2 in the gap ($L_{gap} < 100$ nm). (c) A CNT nanogap device biased in IMT2, corresponding to oscillations of VO_2 in a narrow region below the CNT, but extending along its full length ($L = 3.4$ μm). Despite the larger volume heated and cooled across the IMT, the VO_2 during IMT2 oscillates around 1000 times faster than in IMT1. (d)–(f) are magnified plots of (a)–(c). (g)–(h) With the same setup and devices, but with the current bias applied using a Keithley 2450 instead of a Keithley 4200-SCS source, nearly an order-of-magnitude change in oscillation frequency is produced for the VO_2 and nanogap devices operated in IMT1. (i) The nanogap device in IMT2 is not affected by a change of the current source.

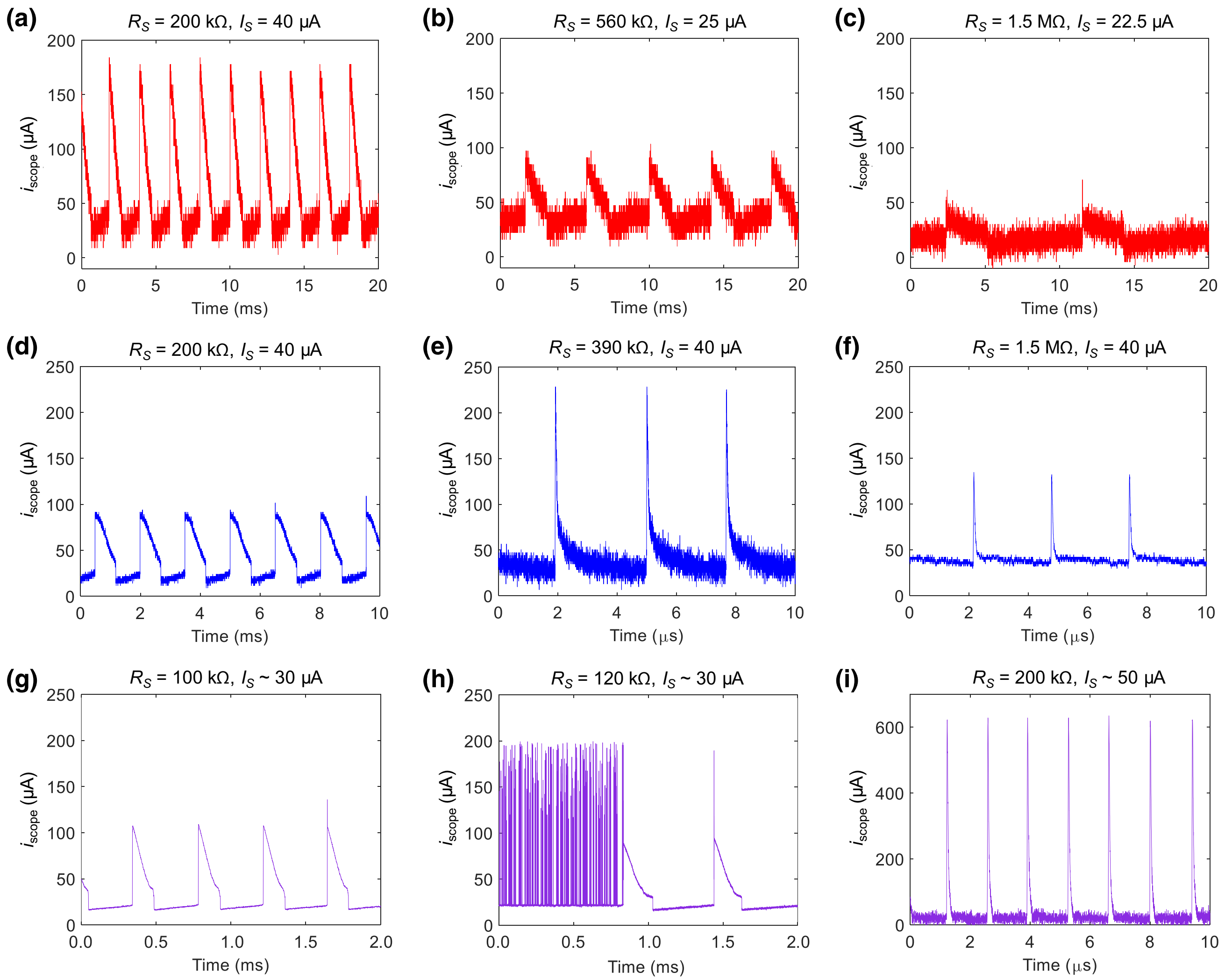

FIG. 4. Effect of the series resistor (R_S) on oscillations. (a)–(c) A micrometer-scale VO_2 device ($L \sim 5$ μm, $W \sim 5$ μm) without a metallic CNT. (d)–(f) A CNT nanogap device biased in IMT2 ($L = 4.7$ μm). (g)–(i) A VO_2 device with a continuous CNT heater ($L = 3.7$ μm). For data acquired on long (millisecond) time scales [in (a)–(d), (g),(h)], the fast rising edge spike is not displayed or is subsampled by the oscilloscope to show a smaller amplitude.

faster. This means that within the same nanogap device's effective circuit, we observe two distinct oscillation frequencies (i.e., that of IMT1 and that of IMT2) three orders of magnitude apart using a current bias differing by less than an order of magnitude.

However, these two oscillation frequencies do not represent two distinct intrinsic device time scales. Rather than being set solely by device size and thermal mass, the spiking frequency of IMT devices can be influenced by electrical capacitances, not only as part of the device contacts or geometry, but also externally from the probe station or current source itself. In our measurements, we observe that, all else being the same (namely, the bias current, cables, series resistor, probes, and the device itself), the choice of current source has a significant impact on the frequency of slow oscillations in a VO_2 device without a CNT [Fig. 3(g)] or a nanogap device in IMT1 [Fig. 3(h)]. In these devices, the use of a Keithley 2450 SourceMeter instead of a Keithley 4200-SCS parameter analyzer to apply the same fixed current results in nearly an order-of-magnitude increase in oscillation frequency. Similarly, increases in current output range settings of either source result in significant slowing of the observed oscillations, even though the same current bias is applied. This appears to arise from changes in effective source capacitance (or other internal instabilities) with source settings, as further explored in Sec. 2(c) and Fig. S7 of the Supplemental Material [24].

In contrast, the faster oscillations of VO_2 devices with a continuous CNT heater [19] and nanogap devices in IMT2 [Fig. 3(i)] are insensitive to, and isolated from, the choice of the current source and its measurement range.

We note that in these megahertz devices, unlike the slow sub-kilohertz ones, oscillations are easily accessible using either a voltage bias (combined with an appropriate value of R_S) or a current bias. The faster frequencies thus appear to be more representative of the device's intrinsic electrical and thermal time scales.

If the changes in total resistance and voltage seen by the current source are small enough, then it may be possible to avoid significantly discharging source capacitors and involving them in the oscillations. Thus, we investigate the effects of changing the series resistor: a large R_S should more effectively isolate the system from external parasitics, while a small R_S should encourage slow oscillations. In large micrometer-sized VO_2 devices [Figs. 4(a)–4(c)], an increase in R_S has minimal impact on oscillation frequency and makes the oscillatory regime occur over a narrower range of currents so it is increasingly hard to access. No fast oscillations are observed for 200 k$\Omega \leq R_S \leq$ 1.5 MΩ, and no stable oscillations are accessible above about 2 MΩ.

As R_S increases, the amplitude of source-driven oscillations in device current generally decreases because the difference in total circuit resistance between insulating ($R_S + R_{VO_2,\text{ins}}$) and metallic states ($R_S + R_{VO_2,\text{met}} \approx R_S$) reduces. For the nanogap devices undergoing IMT1, this makes it difficult to resolve oscillations above the noise floor with larger R_S, especially because these devices have a very small change in resistance during IMT1 even before insertion of R_S.

At small values of R_S, we observe that nanogap devices in IMT2 and continuous CNT heater devices, which behave similarly and are displayed in Figs. 4(d)–4(i), show slow sub-kilohertz oscillations. These oscillations have a similar nature to VO_2 devices without a CNT, and nanogap devices in IMT1, in which the external capacitance is highly influential and sets the effective oscillation frequency. However, the nanogap IMT2 and continuous CNT devices show orders-of-magnitude faster oscillations once shielded from source parasitics at larger R_S. In this regime, the changes to the total circuit resistance ($R_S + R_{\text{device}}$) are smaller and occur over faster time scales than the source and its capacitor can track, resulting in a constant current bias to the device. Further increases to R_S do not significantly alter oscillation frequency. If a critical value of R_S is chosen, the device can become unstable and abruptly switch between fast (megahertz) and slow (kilohertz) oscillations, shown in Fig. 4(h). That is, there does not appear to be a gradual change in oscillation frequency from slow to fast as R_S is tuned, but rather two discrete frequencies.

It remains unclear as to why our micrometer-sized VO_2 devices do not exhibit rapid device dynamics at higher R_S, although this may be related to the form of the NDR and the resistance of the high-current-density channel (metallic state) relative to the surrounding low-current-density (insulating state) VO_2 [29]. The isolation of high-speed internal dynamics in devices with a CNT heater (i.e., a connected nanogap or continuous CNT) has likely been made easier via a decrease in the device's resistance combined with changes to its electrical response to temperature, that is, on the creation and dissolution of the narrow metallic VO_2 conducting channel, and therefore its NDR and associated dynamics. This is discussed as a possibility in Secs. 2(c) and 5 of the Supplemental Material [24], but requires further study.

We find the influence of the source on device oscillation frequency to be a very common issue with measurements made using a fixed current bias, including with commonly used parameter analyzers in research laboratories such as the Agilent B1500 and the Keithley 4200. If oscillation time scales truly originate from the device, then no changes should be observed with the current source (along with associated parasitic capacitances) or its range settings, in addition to increases in the series resistor.

C. Compact modeling of factors influencing oscillation frequency

To gain further insight into the origin of oscillation time scales, we construct a compact model in which oscillations arise from a thermally driven NDR coupled to one of two electrical capacitances: one intrinsic to the device structure, and one within the current source. Furthermore, we show that the circuit dynamics can abruptly switch between excitation of each capacitor, as shown in Fig. 4(h), as a function of an electrical and/or a thermal tuning parameter, such as the external series resistor, the device thermal capacitance, and/or the strength of an added heat source like a CNT.

The device model consists of nonlinear thermally activated Schottky transport for the device [30], coupled to Newton's law of cooling [Eq. (1)], which describes the competition between self-heating and heat loss to the environment. C_{th} is the thermal capacitance (which scales with switching volume), R_{th} is a lumped thermal resistance between the hot device and the environment, T represents an average device temperature, and T_0 is the ambient temperature. i_m and v_m are the current through and voltage across the device, respectively. We examine the effect of scaling C_{th}, as well as the effect of including a resistive heater (R_{heater}), such as the CNT which appears electrically in parallel to the oscillating VO_2 biased at IMT2. This heater adds a Joule heat source term in the thermal dynamics, given as the last term of the following equation:

$$C_{\text{th}}\frac{dT}{dt} = i_m v_m - \frac{T - T_0}{R_{\text{th}}} + \frac{v_m^2}{R_{\text{heater}}}. \tag{1}$$

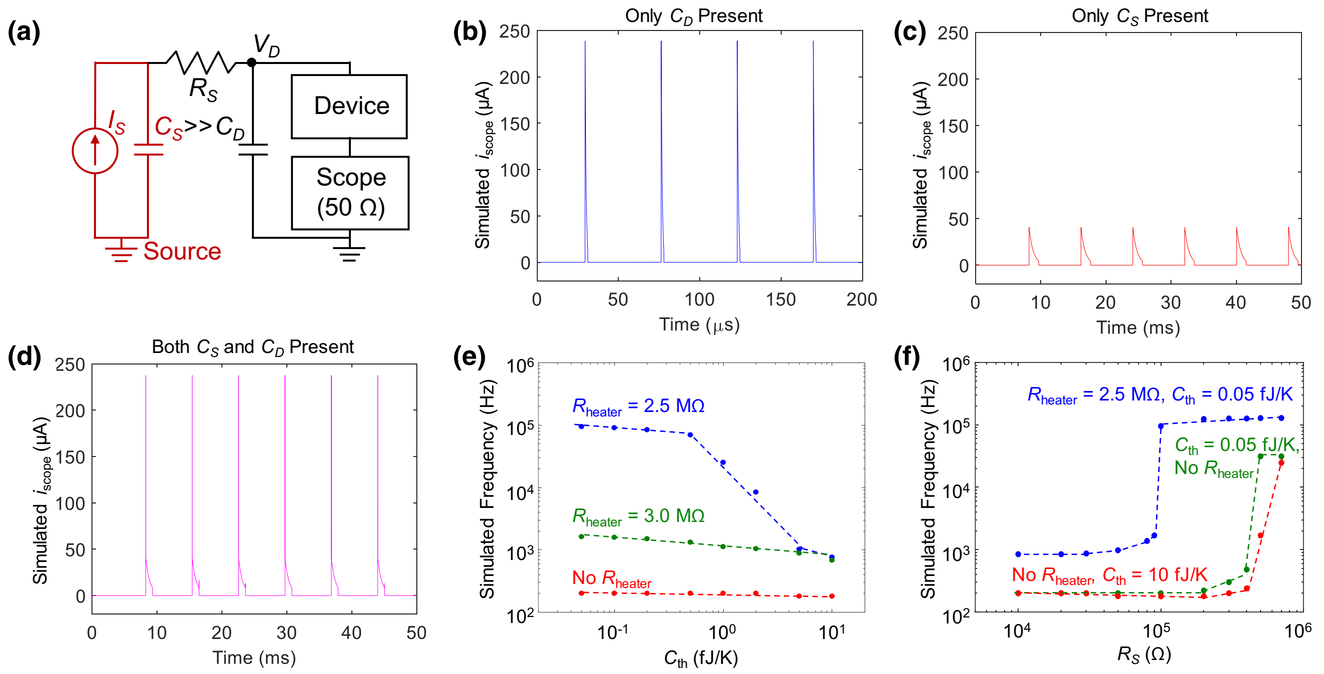

FIG. 5. Modeling of oscillations in a device with a nonlinear thermally driven instability. (a) Schematic of the simulated circuit, including a capacitance C_S associated with external parasitics (i.e., the current source), and a capacitance C_D associated with the device. When held at $I_S = 3$ μA, within a region of NDR, oscillations occur (b) relatively rapidly at around 20 kHz with only C_D present, (c) relatively slowly at around 0.1 kHz with only C_S present, and (d) relatively slowly when both capacitors are in the system. In all three cases, $R_S = 100$ kΩ and $C_{th} = 0.05$ fJ/K, corresponding to a small device volume. (e) Adding a heater with resistance less than 2.5 MΩ and simultaneously reducing C_{th} produces an abrupt frequency increase (blue) by avoiding involvement of C_S. If the device only self-heats (red) or a weaker heater is used (green), then C_{th} has no effect on frequency. (f) Increasing R_S can also abruptly decouple the device dynamics from C_S, allowing a speed-up by a factor of more than 100. Adding a heater shifts the critical crossover point to lower R_S.

This nonlinear dynamical model produces abrupt resistive switching during a dc voltage sweep (due to positive feedback and thermal runaway) and an NDR instability during a current sweep, similar to IMT switching devices. The model approximates the device behavior with mathematically simple Schottky transport, as any sufficiently nonlinear thermal transport will produce volatile switching and NDR (and the associated self-oscillations in a relaxation circuit), although it does not capture all the underlying physics. We do not include an explicit IMT mechanism, instead capturing the switching and NDR with a simpler model to more clearly isolate the effects of electrical capacitance and tuning parameters that lead to dramatic changes in the dynamics.

The switching device model is incorporated into a relaxation oscillator circuit including two capacitors and a series resistor R_S, shown in Fig. 5(a). C_D represents intrinsic device capacitance, whereas C_S represents larger external parasitics like those from a current source or another device in a network. Section 5 of the Supplemental Material includes additional details, as well as an alternative configuration where C_S is instead located as a second large device capacitance [24]. When only $C_D = 30$ pF is present, the system oscillates rapidly at around 20 kHz for fixed $I_S = 3$ μA (held within the region of NDR), shown in Fig. 5(b). When only a large external parasitic $C_S = 5$ nF is present in the system, with fixed $I_S = 3$ μA, oscillations occur slowly at 0.1 kHz [Fig. 5(c)]. If both capacitors are present, then C_S dominates, resulting in low-frequency oscillations in which an initial fast spike is added to the rising edge of each slow spike, shown in Fig. 5(d). The shape of the spikes combines aspects of each electrical time scale, reproducing the behavior of our micrometer-scale VO_2 devices shown in Fig. 3(d).

The difference in duration of the rapidly decaying metallic state (the short spike) compared to the longer insulating state (between spikes) in this model (i.e., the spike spacing) stems largely from the electrical capacitance. When the device is insulating and highly resistive, any electrical time scales are large, and the capacitor charging is slow. With the rapid change in voltage upon switching, the capacitor(s) can more rapidly discharge through the much more conductive metallic device, which then cools quickly. However, we refrain from assigning a single fixed electrical or thermal time constant to either the metallic or insulating state because the device's resistance and heating change considerably throughout the dynamics. For instance, the switching speed of VO_2 is known to vary by

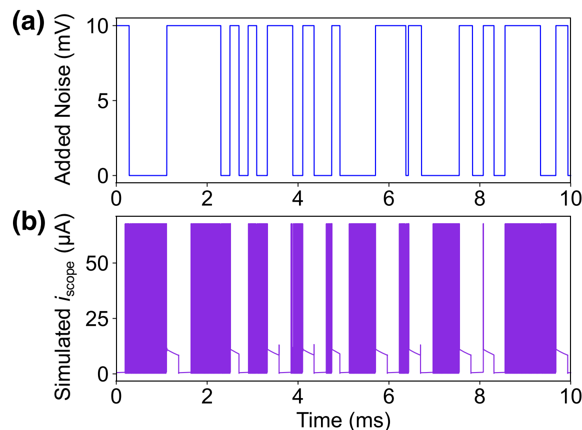

FIG. 6. Modeling of autonomous frequency jumping. Random telegraph noise is added to the device voltage with a 10-mV amplitude and millisecond time scale (upper panel). As a result, the system abruptly jumps between fast and slow oscillations (lower panel). $R_S = 95$ kΩ, $I_S = 5$ μA, $C_{th} = 0.05$ fJ/K.

orders of magnitude depending on the applied voltage (see, for example, incubation curves in Ref. [8] and Fig. S13 in the Supplemental Material [24]), even in a purely thermal simulation with no electrical capacitance. Thus, the long spike spacing is expected to be shorter if the power in the device can be more rapidly increased by reducing electrical capacitance (if limited by an intrinsic C_D, then scaling the device could reduce this), increasing the bias setpoint, or by thermally engineering the device to heat up more for a given input power.

Preventing the larger capacitor from charging and discharging can significantly increase oscillation speed and reduce spike energy. Therefore, we investigate whether certain parameters in our model can alter which of the capacitances dominates the system's dynamics if the large capacitor C_S cannot be removed. To simulate the reduction of switching volume from micrometers to tens of nanometers, we reduce C_{th} by a factor of 1000, but find that the oscillation frequency remains nearly the same [Fig. 5(e)]. Similarly, reducing C_D has no effect on the overall oscillation frequency when C_S remains much larger. As a result, simply scaling the device is likely not enough to speed up oscillations if it does not simultaneously reduce the dominant circuit capacitance.

Instead, adding a sufficiently conductive Joule heater is found to excite C_D and avoid significant cycling of the charge on C_S, producing oscillations up to about 0.1 MHz once C_{th} is sufficiently small, as shown in Fig. 5(e). When the Joule heater is either absent or insufficiently strong, the oscillation frequency remains slow over a large range of C_{th} [Fig. 5(e)]. The combination of small thermal capacitance and an added heat source may make it easier to access faster intrinsic dynamical behavior over those dominated by large external capacitance, as in our nanogap IMT2 devices utilizing a CNT heater.

In addition, we examine the effects of the external series resistor R_S on oscillation frequency. As shown in Fig. 5(f), if R_S is too small then C_S couples into the device dynamics and produces slow sub-kilohertz oscillations. Once R_S is large enough, faster intrinsic dynamics from the interaction with device capacitance C_D are accessible. The transition between the two regimes can be abrupt, with no intermediate oscillation frequency, as is observed in our experiments. Changing C_{th} (such as through device scaling) has minimal effect, but the addition of a heat source R_{heater} pushes the critical value of R_S needed to shift to the faster sub-megahertz oscillation regime to a lower value, making it easier to produce fast spiking in the system.

Thus, a two-capacitor model can reasonably reproduce the time scales and pulse shapes observed in the experiments. The modeling results show that volume scaling can be important for achieving faster oscillations by determining C_{th} and C_D, but should be accompanied by careful control of all circuit capacitances. We find that the largest circuit capacitance, in this case external source capacitance, tends to dominate oscillatory dynamics but does not necessarily do so under all conditions. A means for probing intrinsic oscillations may be provided via the external circuitry (i.e., the series resistor), or by modifying the thermal behavior of the device itself (e.g., using a linear heater), which can change the NDR dynamics involved in oscillations.

D. Compact modeling of frequency hopping

Finally, we demonstrate that the simulated system can autonomously jump between two oscillation frequencies, observed experimentally in Fig. 4(h), when random telegraph noise (RTN) is introduced to the model. Figure 6(a) shows an example of RTN added to the device voltage [V_D in Fig. 5(a)], with amplitude 10 mV and a time scale of the order of 1 ms. This could represent noise arising from the device resistance or capacitance, such as from traps in either the CNT or the VO_2 [31,32], or perhaps from stochastic switching of small VO_2 domains (e.g., from percolation at the edges of the metallic VO_2 region or from defects with a different local T_{IMT}) [33,34]. When the system is operated in the presence of RTN with R_S near the crossover value at 95 kΩ in Fig. 5(f), oscillations repeatedly hop between the two frequencies, as shown in Fig. 6(b). Without RTN the system oscillates rapidly, but when the voltage V_D suddenly increases the system switches to slow oscillations, at least temporarily. At values of R_S far from the crossover value, here below about 80 kΩ or above about 110 kΩ, the system is unaffected by the RTN and oscillates uniformly slowly or rapidly.

Frequency hopping is observed using very small RTN amplitudes, less than 1% of the voltage V_D, and is still observed at amplitudes below 0.5 mV. As the noise amplitude reduces, the range of R_S values over which hopping is

observed shrinks, while at larger noise amplitudes fluctuations in the frequency within the slow or fast oscillations begin to be visible even when hopping does not occur. In contrast, white noise will not produce any of these effects. Similar frequency hopping is observed if RTN is added to the Joule heating process, in the value of R_{heater} in Eq. (1) or to the value of R_{th}, rather than to electrical noise on V_D. Fluctuations in these resistances of less than 1% will produce hopping behavior. Such nonlinear devices are thus highly sensitive to perturbations and instabilities when operated near crossover points.

III. CONCLUSION

In conclusion, the spiking speed of a VO_2-based Mott oscillator, and the dynamical time scales of nonlinear thermally driven oscillators in general, are not strictly determined by device geometry alone. Here, we report on how different capacitors, both intrinsic and extrinsic to a device, can influence the measured time scales of oscillatory dynamics. We find that capacitance and/or instability in the current source used to bias the device can complicate measurements of oscillations, giving rise to much slower dynamics than the device is inherently capable of. Influence of a current source can be identified by changes in response to the source used, its range settings, or the external series resistor used. However, by using a larger series resistor or by thermally engineering the device dynamics, it may be possible to avoid excitation of a large external capacitor. The construction of the electrical control circuit is therefore an important consideration in establishing and controlling the dynamics of nonlinear devices, in addition to engineering the electrical and thermal time scales of the device itself.

ACKNOWLEDGMENTS

H.S. Philip Wong is gratefully acknowledged for providing technical advice. Device fabrication was performed at the Stanford Nanofabrication Facility and the Stanford Nano Shared Facilities, supported by the National Science Foundation (NSF) under award ECCS-1542152. This work was supported in part by ON Semiconductor, by the Stanford SystemX Alliance, and by the X-Grants Program of the President's Excellence Fund at Texas A&M University. S.B. and M.I. acknowledge support from the Stanford Graduate Fellowship (SGF) program, and S.B. from the NSERC Postgraduate Scholarship program. S.K. acknowledges the Laboratory Directed Research and Development program at Sandia National Laboratories, a multimission laboratory operated for the US Department of Energy (DOE)'s National Nuclear Security Administration under contract DE-NA0003525. This paper describes objective technical results and analyses. Any subjective views or opinions that might be expressed in the paper do not necessarily represent the views of the US Department of Energy or the United States Government. R.S.W. acknowledges the X-Grants Program of the President's Excellence Fund at Texas A&M University.

[1] A. Raychowdhury, A. Parihar, G. H. Smith, V. Narayanan, G. Csaba, M. Jerry, W. Porod, and S. Datta, Computing with networks of oscillatory dynamical systems, Proc. IEEE **107**, 73 (2019).

[2] D. E. Nikonov and I. A. Young, Benchmarking delay and energy of neural inference circuits, IEEE J. Explor. Solid-State Comput. Devices Circuits **5**, 75 (2019).

[3] A. A. Sharma, Y. Li, M. Skowronski, J. A. Bain, and J. A. Weldon, High-frequency TaO_x-based compact oscillators, IEEE Trans. Electron Devices **62**, 3857 (2015).

[4] A. A. Sharma, Y. Kesim, J. A. Bain, M. Skowronski, and J. A. Weldon, in *2016 Solid State Devices and Materials International Conference*, pp. 26.

[5] Y. Zhou and S. Ramanathan, Mott memory and neuromorphic devices, Proc. IEEE **103**, 1289 (2015).

[6] W. Yi, K. K. Tsang, S. K. Lam, X. Bai, J. A. Crowell, and E. A. Flores, Biological plausibility and stochasticity in scalable VO_2 active memristor neurons, Nat. Commun. **9**, 4661 (2018).

[7] J. L. Andrews, D. A. Santos, M. Meyyappan, R. S. Williams, and S. Banerjee, Building brain-inspired logic circuits from dynamically switchable transition-metal oxides, Trends Chem. **1**, 711 (2019).

[8] D. Li, A. A. Sharma, D. K. Gala, N. Shukla, H. Paik, S. Datta, D. G. Schlom, J. A. Bain, and M. Skowronski, Joule heating-induced metal-insulator transition in epitaxial VO_2/TiO_2 devices, ACS Appl. Mater. Interfaces **8**, 12908 (2016).

[9] S. Kumar, Z. Wang, N. Davila, N. Kumari, K. J. Norris, X. Huang, J. P. Strachan, D. Vine, A. L. D. Kilcoyne, Y. Nishi, and R. S. Williams, Physical origins of current and temperature controlled negative differential resistances in NbO_2, Nat. Commun. **8**, 658 (2017).

[10] Y. Taketa, F. Kato, M. Nitta, and M. Haradome, New oscillation phenomena in VO_2 crystals, Appl. Phys. Lett. **27**, 212 (1975).

[11] Y. W. Lee, B.-J. Kim, J.-W. Lim, S. J. Yun, S. Choi, B.-G. Chae, G. Kim, and H.-T. Kim, Metal-insulator transition-induced electrical oscillation in vanadium dioxide thin film, Appl. Phys. Lett. **92**, 162903 (2008).

[12] M. D. Pickett, G. Medeiros-Ribeiro, and R. S. Williams, A scalable neuristor built with Mott memristors, Nat. Mater. **12**, 114 (2013).

[13] M. D. Pickett and R. S. Williams, Sub-100 fJ and sub-nanosecond thermally driven threshold switching in niobium oxide crosspoint nanodevices, Nanotechnology **23**, 215202 (2012).

[14] A. Beaumont, J. Leroy, J. C. Orlianges, and A. Crunteanu, Current-induced electrical self-oscillations across out-of-plane threshold switches based on VO_2 layers integrated in crossbars geometry, J. Appl. Phys. **115**, 154502 (2014).

[15] J. Del Valle, P. Salev, Y. Kalcheim, and I. K. Schuller, A caloritronics-based Mott neuristor, Sci. Rep. **10**, 4292 (2020).

[16] B. Zhao and J. Ravichandran, Low-Power Microwave Relaxation Oscillators Based on Phase-Change Oxides for Neuromorphic Computing, Phys. Rev. Appl. **11**, 014020 (2019).

[17] F. Xiong, A. D. Liao, D. Estrada, and E. Pop, Low-power switching of phase-change materials with carbon nanotube electrodes, Science **332**, 568 (2011).

[18] J. Lin, S. Guha, and S. Ramanathan, Vanadium dioxide circuits emulate neurological disorders, Front. Neurosci. **12**, 856 (2018).

[19] S. M. Bohaichuk, S. Kumar, G. Pitner, C. J. McClellan, J. Jeong, M. G. Samant, H.-S. P. Wong, S. S. P. Parkin, R. S. Williams, and E. Pop, Fast spiking of a Mott VO_2-carbon nanotube composite device, Nano Lett. **19**, 6751 (2019).

[20] H. J. Wan, P. Zhou, L. Ye, Y. Y. Lin, T. A. Tang, H. M. Wu, and M. H. Chi, In situ observation of compliance-current overshoot and its effect on resistive switching, IEEE Electron Device Lett. **31**, 246 (2010).

[21] N. Patil, A. Lin, E. R. Myers, R. Koungmin, A. Badmaev, Z. Chongwu, H. S. P. Wong, and S. Mitra, Wafer-scale growth and transfer of aligned single-walled carbon nanotubes, IEEE Trans. Nanotechnol. **8**, 498 (2009).

[22] S. M. Bohaichuk, M. Muñoz Rojo, G. Pitner, C. J. McClellan, F. Lian, J. Li, J. Jeong, M. G. Samant, S. S. P. Parkin, H.-S. P. Wong, and E. Pop, Localized triggering of the insulator-metal transition in VO_2 using a single carbon nanotube, ACS Nano **13**, 11070 (2019).

[23] J. Jeong, N. Aetukuri, T. Graf, T. D. Schladt, M. G. Samant, and S. S. P. Parkin, Suppression of metal-insulator transition in VO_2 by electric field-induced oxygen vacancy formation, Science **339**, 1402 (2013).

[24] See Supplemental Material at http://link.aps.org/supplemental/10.1103/PhysRevApplied.19.044028 for further information about fabrication, modeling details, as well as additional electrical and scanning probe measurements.

[25] S. Sadewasser and T. Glatzel, *Kelvin Probe Force Microscopy: Measuring and Compensating Electrostatic Forces* (Springer, Berlin, 2011).

[26] Y. Zhang, W. Zhu, F. Hui, M. Lanza, T. Borca-Tasciuc, and M. Muñoz Rojo, A review on principles and applications of scanning thermal microscopy (SThM), Adv. Funct. Mater. **30**, 1900892 (2019).

[27] E. Puyoo, S. Grauby, J. M. Rampnoux, E. Rouviere, and S. Dilhaire, Thermal exchange radius measurement: application to nanowire thermal imaging, Rev. Sci. Instrum. **81**, 073701 (2010).

[28] X. Liu, S. Li, S. K. Nandi, D. K. Venkatachalam, and R. G. Elliman, Threshold switching and electrical self-oscillation in niobium oxide films, J. Appl. Phys. **120**, 124102 (2016).

[29] S. K. Nandi, S. K. Nath, A. E. El-Helou, S. Li, X. Liu, P. E. Raad, and R. G. Elliman, Current localization and redistribution as the basis of discontinuous current controlled negative differential resistance in NbO_x, Adv. Funct. Mater. **29**, 1906731 (2019).

[30] G. A. Gibson, Designing negative differential resistance devices based on self-heating, Adv. Funct. Mater. **28**, 1704175 (2018).

[31] F. Liu, K. L. Wang, C. Li, and C. Zhou, Study of random telegraph signals in single-walled carbon nanotube field effect transistors, IEEE Trans. Nanotechnol. **5**, 441 (2006).

[32] F. Liu, K. L. Wang, D. Zhang, and C. Zhou, Random telegraph signals and noise behaviors in carbon nanotube transistors, Appl. Phys. Lett. **89**, 243101 (2006).

[33] M. Jerry, K. Ni, A. Parihar, A. Raychowdhury, and S. Datta, Stochastic insulator-to-metal phase transition-based true random number generator, IEEE Electron Device Lett. **39**, 139 (2018).

[34] A. Frenzel, M. M. Qazilbash, M. Brehm, B.-G. Chae, B.-J. Kim, H.-T. Kim, A. V. Balatsky, F. Keilmann, and D. N. Basov, Inhomogeneous electronic state near the insulator-to-metal transition in the correlated oxide VO_2, Phys. Rev. B **80**, 115115 (2009).

Supplemental Material

Intrinsic and Extrinsic Factors Influencing Dynamics of VO_2 Mott Oscillators

Stephanie M. Bohaichuk,[1*] Suhas Kumar,[2*] Mahnaz Islam,[1] Miguel Muñoz Rojo,[1,3] R. Stanley Williams,[4] Gregory Pitner,[1] Jaewoo Jeong,[5] Mahesh G. Samant,[5] Stuart S. P. Parkin,[5] Eric Pop[1,6]

[1]*Dept. of Electrical Engineering, Stanford University, Stanford, CA, USA*
[2]*Sandia National Laboratories, Livermore, CA, USA*
[3]*Dept. of Thermal and Fluid Engineering, University of Twente, Enschede, The Netherlands*
[4]*Dept. of Electrical & Computer Engineering, Texas A&M University, College Station, TX, USA*
[5]*IBM Almaden Research Center, San Jose, CA, USA*
[6]*Dept. of Materials Science and Engineering, Stanford University, Stanford, CA, USA*
Email: sbohaichuk@alumni.stanford.edu (S.M.B.), su1@alumni.stanford.edu (S.K.)

Supplemental Material Contents:

1. Device Fabrication
    a. How to Cut a CNT
    b. How Not to Cut a CNT
2. Electrical Measurements
    a. DC Electrical Characterization
    b. Oscillations
    c. Impact of the Current Source on Oscillations
    d. Impact of the Series Resistor (R_S) on Oscillations
    e. Temperature Dependence
    f. Incubation Time and Switching Energy
3. Additional Scanning Probe Microscopy Measurements
    a. Kelvin Probe Microscopy
    b. Scanning Thermal Microscopy
4. Finite Element Modeling
5. Compact Modeling in LT Spice
6. Video
7. LT Spice Files

1. Device Fabrication

A finished device schematic is shown in Fig. 1a of the main text. To achieve this device structure, thin films of vanadium dioxide (VO_2) were first grown epitaxially on single crystal TiO_2 (101) substrates by pulsed laser deposition [22]. Films were smooth (<1 Å rms roughness), with a slight self-limiting surface oxidation to V_2O_5. The VO_2 exhibited transition temperatures of 328 K during heating (insulator to metal, T_{IMT}) and 321 K during cooling (metal to insulator, T_{MIT}), with a change in resistance over three orders of magnitude [21].

Separately, carbon nanotubes (CNTs) were grown by chemical vapour deposition on an ST-cut quartz substrate using Fe nanoparticles as catalysts, in order to achieve horizontal alignment of the CNTs [20]. The resulting CNTs were a mixture of metallic and semiconducting, with an average diameter of 1.2 nm and an average lateral density of 1 CNT per 3 µm. The CNTs were transferred onto the surface of the VO_2, using 100 nm e-beam evaporated Au as a sacrificial support layer [20,21]. The Au/CNTs were peeled off the quartz using thermal release tape, and then pressed onto the VO_2. The tape was removed at 130ºC; then Ar and O_2 plasma cleans were done to remove any tape residue off the Au. Finally, the Au was wet etched in a KI solution to leave aligned CNTs on the VO_2. Some carbon-based residue was left behind in the process. (See also Ref. [21])

The VO_2 was patterned into stripes of width W = 2 to 10 µm, with CNTs outside the patterned stripes removed by a light O_2 plasma prior to wet etching the VO_2 in 25% nitric acid [21]. Contacts with spacing L = 3 to 8 µm were made of 50 nm e-beam evaporated Pd (no adhesion layer was used) that was patterned using lift-off. The CNT and the VO_2 are electrically in parallel, sharing the same contacts. After processing, the VO_2 thickness was measured to be ~ 5 nm.

Devices with a metallic CNT were identified electrically (a VO_2 device with a metallic CNT will carry noticeably more current than a device with insulating VO_2 alone) [21], and the number of CNTs was confirmed using atomic force microscopy (AFM). Devices with a single metallic CNT were the focus of this study, as shown schematically in Fig. 1a in the main text.

a. How to Cut a CNT

To create nanogaps (see Figs. 1 and S1), a metallic CNT within a device was cut using the force of a sharp atomic force microscopy (AFM) tip in lithography mode on a Park XE-100 or an Asylum Research MFP-3D system. Lithography mode is a variation of contact mode with a higher setpoint (a higher force applied to the tip), used to locally indent or scratch the sample rather than image it. CNTs were mechanically cut to form the nanogap rather than patterned via e-beam lithography and etched (i.e., via Ar or O_2 plasma) in order to avoid damage or stoichiometry changes to the underlying VO_2.

For increased hardness and durability, either diamond tips (D300 from K-Tek Nanotechnology, ~40 N/m spring constant, ~300 kHz resonant frequency, 5-10 nm radius), or diamond-like-carbon (DLC) coated Si tips (TAP300DLC from Budget Sensors, ~40 N/m spring constant, ~300 kHz resonant frequency, <15 nm radius) were used.

Care was taken to ensure that the setpoint was high enough to cut the CNT but not so high as to deeply scratch the VO_2 underneath. For cuts, a setpoint of 0.7 V was used with a speed of 0.2 – 20 µm/s. Because the CNTs were only held to the VO_2 surface by Van der Waals forces, they were susceptible to being "dragged" by the tip rather than cut. The two most successful methods of cutting a CNT were:

i) By using several small back-and-forth cuts in rapid sequence (a sawing action) with high force. Cut lines should be very short to minimize lateral force and drag distance. This was used for the devices shown in Figs. 1 and S1b.

ii) By first “stabbing” the CNT (performing a force-distance curve), using a high setpoint such as 1.8 – 2 V. This does not usually break the CNT but weakens it. A cut line can then be done at or just next to the indent point, causing the CNT to snap. This was used for the device in Figs. S1a and S1c.

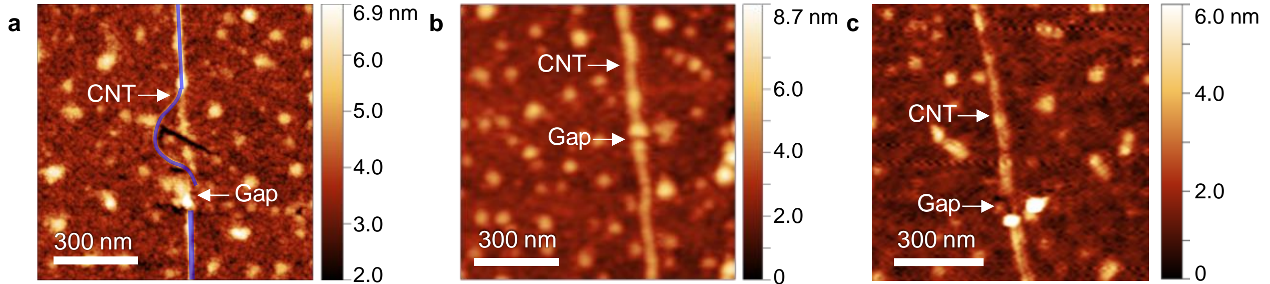

FIG. S1. (a) A cut CNT (marked in blue) within a VO_2 device (L = 4.7 µm, W = 5.0 µm), made by first weakening the CNT and then pulling on it to snap it (there is a scratch in the VO_2 near the bent part of the CNT from the AFM tip scan line used to pull on the CNT). (b) A cut CNT within a VO_2 device (L = 3.7 µm, W = 7.2 µm) made with a small cutting action of the AFM tip. (c) A cut CNT within a VO_2 device (L = 6.5 µm, W = 5.5 µm) made by repeatedly “stabbing” the CNT. The tall particles are carbon-based residue leftover from the CNT transfer process.

b. How Not to Cut a CNT

Small nanogaps (20 – 300 nm) can be created in metallic carbon nanotubes by electrical breakdown [17] on insulating SiO_2 (on Si) substrates. When sufficient bias is applied to the CNT, self-heating causes the CNT to reach its oxidation temperature ~ 600℃ [35]. Since the temperature is not uniform along the CNT (it is hottest in the middle of its length or at a defect site) a gap can be created at a hot spot, which is highly localized if done in an environment with reduced but non-zero oxygen content.

However, the IMT temperature for VO_2 (~55℃) is far lower than 600℃, and therefore devices switch before the CNT gets hot enough to oxidize. Because of the series resistor (current compliance) used, which is necessary to prevent total device failure, the voltage across the CNT abruptly reduces once IMT occurs. The CNT is thus never able to reach a high enough voltage and therefore temperature to form a nanogap by oxidation.

We also tried forming gaps in CNTs by doing local oxidation lithography. This is a scanning probe technique in which a biased AFM tip induces oxidation underneath the tip by a reaction of the sample with adsorbed water normally present on sample surfaces in air [36]. Oxidation was done at a humidity of 75 – 80%, a tip bias of around -1.9 V, and a setpoint of 0.3 V. However, it was found that VO_2 was more susceptible to oxidation than CNTs, and a line of oxide would be formed on the VO_2 before a clear gap was made in the CNT. In other words, at best the CNT simply became more resistive rather than broken.

2. Electrical Measurements

Electrical measurements were performed using a Keithley 4200-SCS parameter analyzer in a Janis Research probe station (ST-100-UHT-4). VO_2 devices with no CNT or with a continuous uncut CNT can be measured equally well in air or vacuum. However, VO_2 devices with a cut CNT had to be measured in vacuum (<10^{-4} Torr), as the defective cut ends are more susceptible to oxidation. Unless otherwise specified all measurements were performed at an ambient temperature T_0 = 295 K.

For all measurements, including scanning probe measurements, a 200 kΩ resistor was used in series with the device as a current compliance in the metallic state (to avoid overheating and failure) unless

otherwise specified. This resistor was added on the probe positioner, right next to the probe tip [21], as close as possible to the device to minimize capacitive current overshoot [24].

a. DC Electrical Characterization

Measurements of the device in main text Fig. 1 before and after cutting the metallic CNT are shown in Fig. S2. Before cutting, the CNT acts as a nanoscale heater triggering a single IMT event in the VO_2 directly underneath. After the nanogap is formed in the CNT, another IMT is introduced at a lower voltage (IMT1), corresponding to IMT of the VO_2 within the nanogap. The second IMT (IMT2) occurs as for the uncut CNT, and corresponds to the IMT of the entire VO_2 "sleeve" below the CNT. However, the total device current is reduced, and the switching voltage increased slightly, due to the added resistance of the VO_2 in the nanogap, and the resistance of the CNT-VO_2 interfaces.

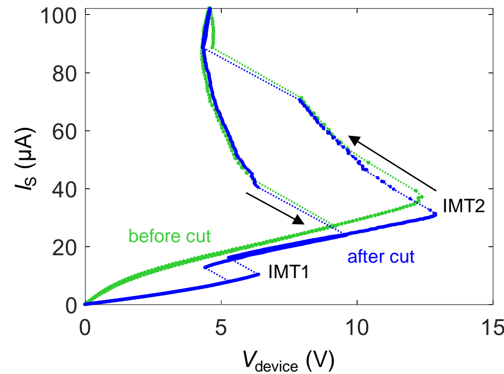

FIG. S2. DC voltage-source switching of the nanogap device in the main text (Figs. 1b-1c with $L = 3.4$ µm, $W = 6.3$ µm) before (green) and after (blue) the CNT is cut using an AFM tip.

DC voltage-source measurements of additional gap devices are shown in Fig. S3, corresponding to the devices shown in Fig. S1. V_{device} refers to the voltage across the Pd contacts to the CNT electrodes and is given by $V_{device} = V_S - I_S R_S$, subtracting the voltage drop across the series resistor from the source voltage V_S. Because there is a significant resistance to the CNT (which is several µm long) in series with the gap, the voltage drop across the VO_2 within the gap will be smaller than V_{device}. Switching in all nanogap devices occurs in two steps, with the gap undergoing IMT (IMT1), then the connected CNT heater triggering an IMT along its length (IMT2). IMT2 occurs at nearly the same voltage as before cutting the CNT.

The on/off ratio of IMT1 (the change in the current just before and after IMT1) is typically only 1.1 – 1.6. When the gap is insulating, nearly half of the total current comes from the parallel leakage current through the VO_2 (far from the gap, between the Pd contacts), which is several µm wide. Once the gap is metallic, the total current is limited by the resistance of the long CNT electrodes. The total current after IMT1 is slightly lower than before cutting the CNT, due to the added interfacial resistance between the CNT ends and the VO_2 underneath, and because metallic VO_2 is slightly more resistive than an equivalent length of metallic CNT. The on/off ratio could thus be increased by making the VO_2 narrower around the CNT (here limited by optical lithography and the wet etching process), and the total CNT length shorter.

The IMT1 voltage can depend slightly on the bias direction and polarity, as shown in Fig. S4. This may reflect some asymmetry in the current flow pathway, or in the interfaces between the CNT ends and the VO_2 (either in their heating, or their contact resistance). The asymmetry may be stronger in devices that have a bent CNT end (Fig. S4a-S4b) compared to a gap device with a straight cut (Fig. S4c), though the higher switching voltage does not always correspond to biasing the side of the CNT that was bent/dragged.

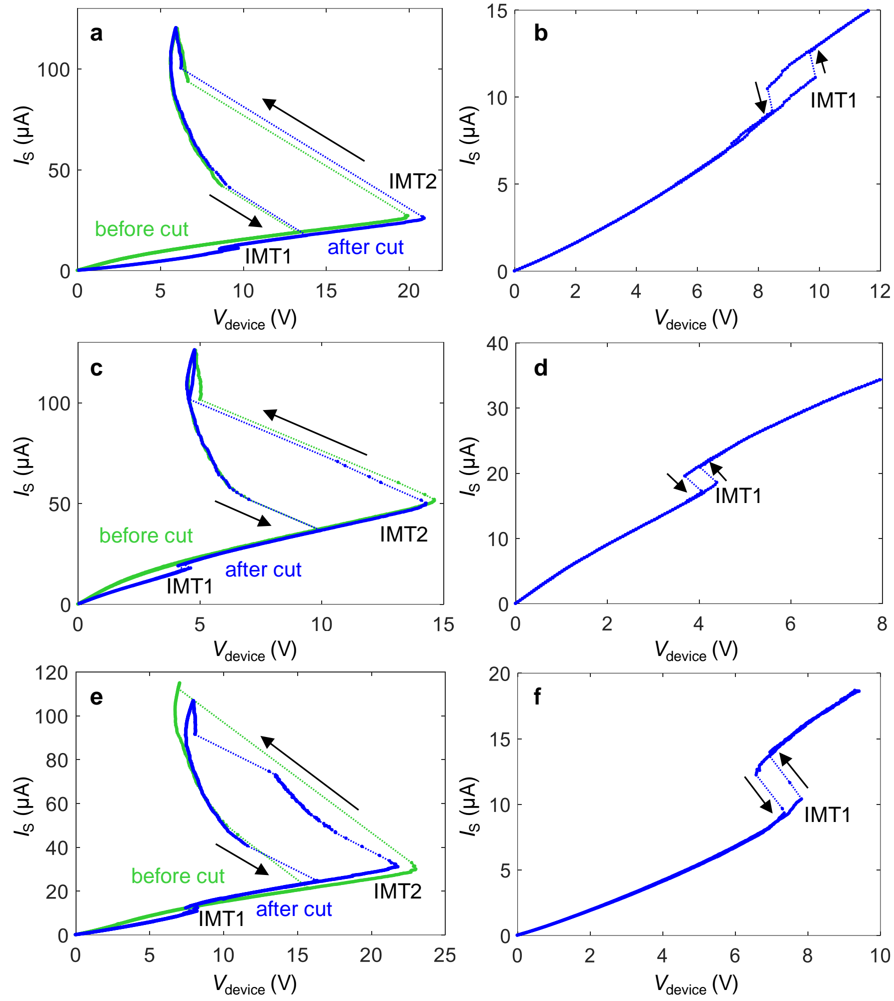

FIG. S3. (a)-(b) DC voltage-source switching of the nanogap device shown in Fig. S1a. Cutting the CNT adds IMT1 associated with the IMT of VO_2 within the gap of the cut CNT. (c)-(d) DC voltage-controlled switching of the gap device shown in Fig. S1b. (e)-(f) DC voltage-controlled switching of the gap device shown in Fig. S1c.

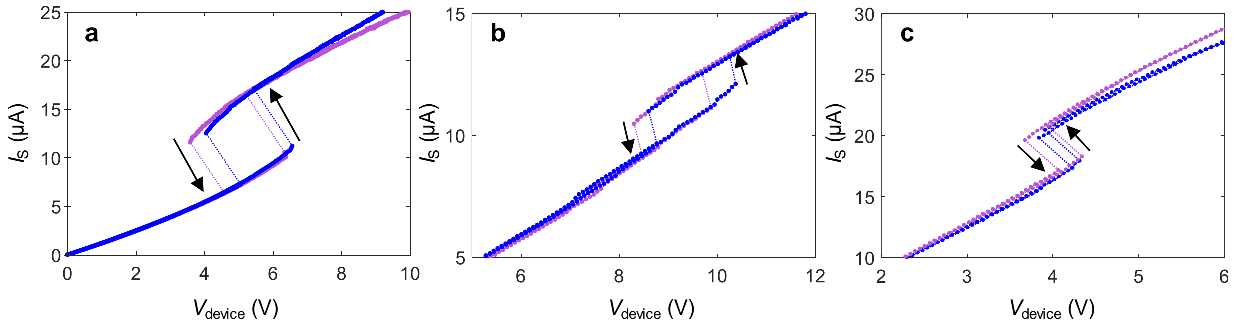

FIG. S4. DC voltage-source measurements of IMT1 in nanogap devices with different bias directions. Relative to the AFM scan images in Fig. S1, a positive bias is applied to the top half of the CNT (purple) or the bottom half (blue). (a) The device in main text Fig. 1 has a slightly higher switching voltage when biased on the bent side. (b) The device in Fig. S1a has a slightly higher switching voltage when the straight side is biased. (c) Switching behavior of the device in Fig. S1b has only very slight directional dependence.

b. Oscillations

Oscillations in device current were measured using an Agilent InfiniiVision MSO710A oscilloscope in series with the device by measuring the voltage across its 50 Ω input impedance. The noise level of the oscilloscope is around 1-2 mV, limiting sensitivity to changes in current close to ~μA range (in addition to background noise, the analog-to-digital converter within the oscilloscope limits output to discrete levels with a maximum resolution of 8-12 levels per 2 mV). Typical measured noise is shown in Fig. S5a. Any offset from 0 V is corrected. This level of noise is observed in measurements of the nanogap device across both IMT1 and IMT2, as well as in VO_2 devices without any CNT. Despite the appearance of different noise levels in main text Fig. 3, which is due to differences in the total voltage range (a higher range limits resolution) and time scales (different sampling density) used, a similar level of noise is observed in all devices. This noise appears to originate from the background/setup and oscilloscope limitations, and not the device itself.

Raw data without any smoothing or filtering is shown in Fig. S5b for the device shown in the main text (Figs. 1 and 3b). Oscillations can be seen more clearly by smoothing the data (red), such as by taking a moving average, here over a window of 20 data points (the spacing between each data point is 1 μs). For comparison, a smoothed noise waveform is shown in red in Fig. S5a, showing no oscillations. The oscilloscope also has a built-in "high resolution" mode which behaves similarly to the post-processing smoothing applied in Fig. S5, in which extra sampled data points are averaged over.

Data can be filtered in hardware during measurements by using the built-in bandwidth limiter on the oscilloscope, which attenuates high frequency noise (approximately >20 MHz). The results of this are shown in Fig. 3b and Fig. S5c, making the oscillations much clearer. A smoothed waveform calculated for this data is also shown in red. Oscillations shown in the main text for the nanogap device (Fig. 3b) were collected simultaneously using the bandwidth limiter and the high resolution mode on the oscilloscope.

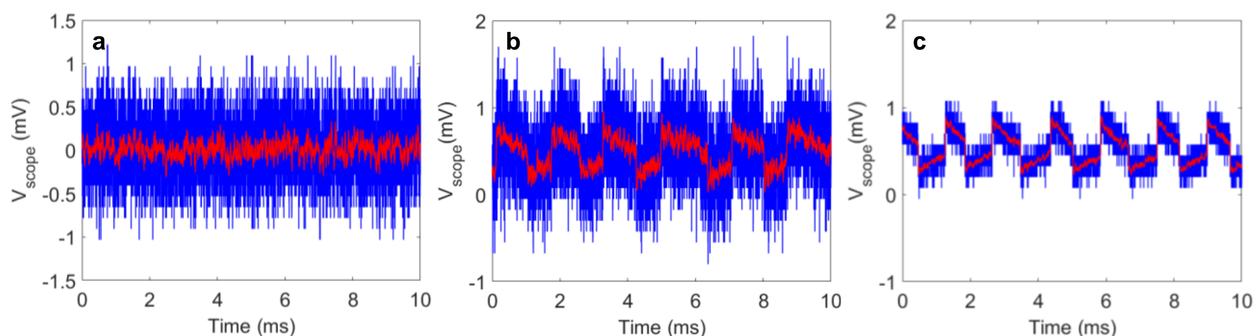

FIG. S5. (a) Typical noise seen by the oscilloscope (blue). A smoothed waveform (red) is generated by taking a moving average. (b) Oscillations corresponding to main text Fig. 3b, without any oscilloscope filtering applied (blue). A smoothed waveform (red) is made by taking a moving average. (c) Oscillations in the same device, measured with the bandwidth limiter on the oscilloscope used (blue). This significantly reduces high frequency noise. A waveform post-processed with a moving average is shown in red.

The energy per pulse delivered to the 50 Ω oscilloscope load is ~3 pJ/pulse and ~0.9 pJ/pulse for oscillations across IMT1 and IMT2, respectively (main text Figs. 3b and 3c). Despite the large differences in pulse duration and magnitude, the total energy delivered to the load for the two types of oscillations is similar. Note that the energy dissipated at the device itself will be different than at the load. Both values are nearly 100 times smaller than the energy delivered to the load per pulse of a similar VO_2 device without any CNT heater or electrode.

We observed oscillations in several other nanogap devices during IMT1 at a similar slow ~kHz frequency, shown in Fig. S6. Fig. S6b corresponds to the device in Fig. S1b, which had an even smaller gap size than the one shown in the main text. However, the on/off ratios of IMT1 in these devices are

smaller than the one presented in the main text, so the amplitude of oscillations and the signal-to-noise ratio are both lower.

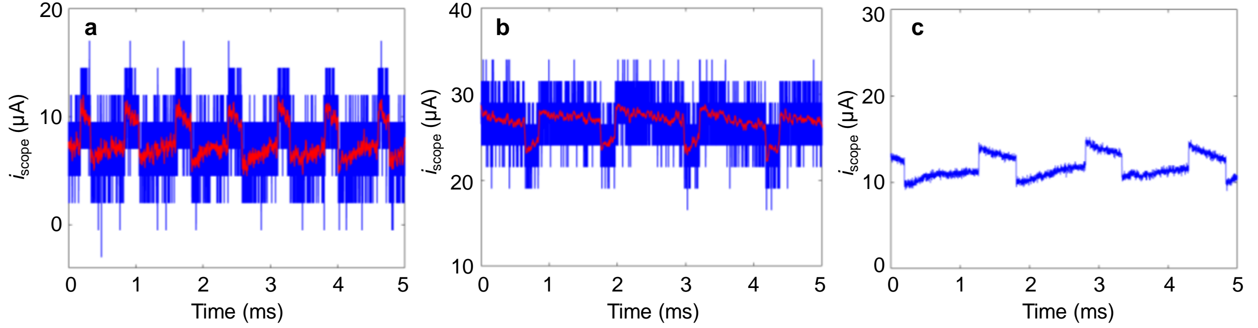

FIG. S6. Oscillations using the bandwidth limiter of the oscilloscope (blue), with a smoothed waveform shown in red, for the nanogap devices (a) shown in Figs. S1a and S3b, at T_0 = 295 K, (b) shown in Figs. S1b and S3d, at T_0 = 284 K, and (c) shown in Figs. S1c and S3f, at T_0 = 296 K. The waveform in panel c also uses the high-resolution mode of the oscilloscope.

c. Impact of the Current Source on Oscillations

As discussed in the main text, the choice of current source and its settings used to apply a fixed bias current can influence and limit the oscillation frequency of IMT devices. For a given current source, the oscillation frequency of two-terminal VO_2 devices was found to decrease by ~2-3× with each decade of increase in the source's output current range setting (100 μA, 1 mA, and 10 mA), even though the same 17 μA bias was applied, shown in Figs. S7a-S7c. We observed this effect in VO_2 devices regardless of whether a Keithley 4200, a Keithley 2450, or an Agilent B1500 was used as a current source. Similar behavior occurred in nanogap devices during the slow oscillations of IMT1 (Figs. S7d-S7f). All oscillations presented in the rest of the paper were obtained using the lowest possible current range for a given bias current, which produces the fastest oscillations.

Changes in the choice of current source and its settings reflect differences in the active feedback circuit and/or in the parasitics. On the one hand, an IMT event causes device resistance to abruptly change, and therefore both the total voltage and load seen by the current source rapidly change. Many parameter analyzers and current sources contain feedback to maintain current levels, and the source may try to respond to the changing load conditions, in turn influencing the dynamical behaviour of the device. On the other hand, the source also contains parasitics, primarily output capacitance(s), that could influence dynamics and ultimately limit their maximum frequency.

To see if the change in current source range is associated with a change in its effective output capacitance, we measured the transient rise in current when the source was turned on to a simple R = 200 kΩ resistive load (no device was present, but the setup was otherwise the same as if there was, with the 50 Ω oscilloscope in series) providing a 100 μA current. The turn-on was not an abrupt step function but rose exponentially with a finite time constant $\tau \sim RC$ due to the system's capacitance. Fitting to this rise time allowed us to extract an approximation for this capacitance, which is on the order of a few nF (Figs. S7g-S7i) and increases with the source range. We note that the value of the extracted C appears dependent on the load (the value of R), as does the shape of the rise time in some cases at smaller R, suggesting that C is an effective output capacitance of a more complex circuit. Given the substantial impact of the source range on C, it is expected that the dominant source of capacitance in the system is from the current source itself (rather than from cables, probes, etc.). The frequency of the slow oscillations in VO_2 devices and IMT1 nanogap devices scales proportionally with the inverse of this capacitance C, as shown in Fig. S8, suggesting that the source may dominate the long spike decay times and spike spacings in the slowly

oscillating (sub-kHz) VO_2 devices. The implementation of the current source circuit can therefore be an important consideration for, as well as a means of control over, oscillatory devices for practical applications.

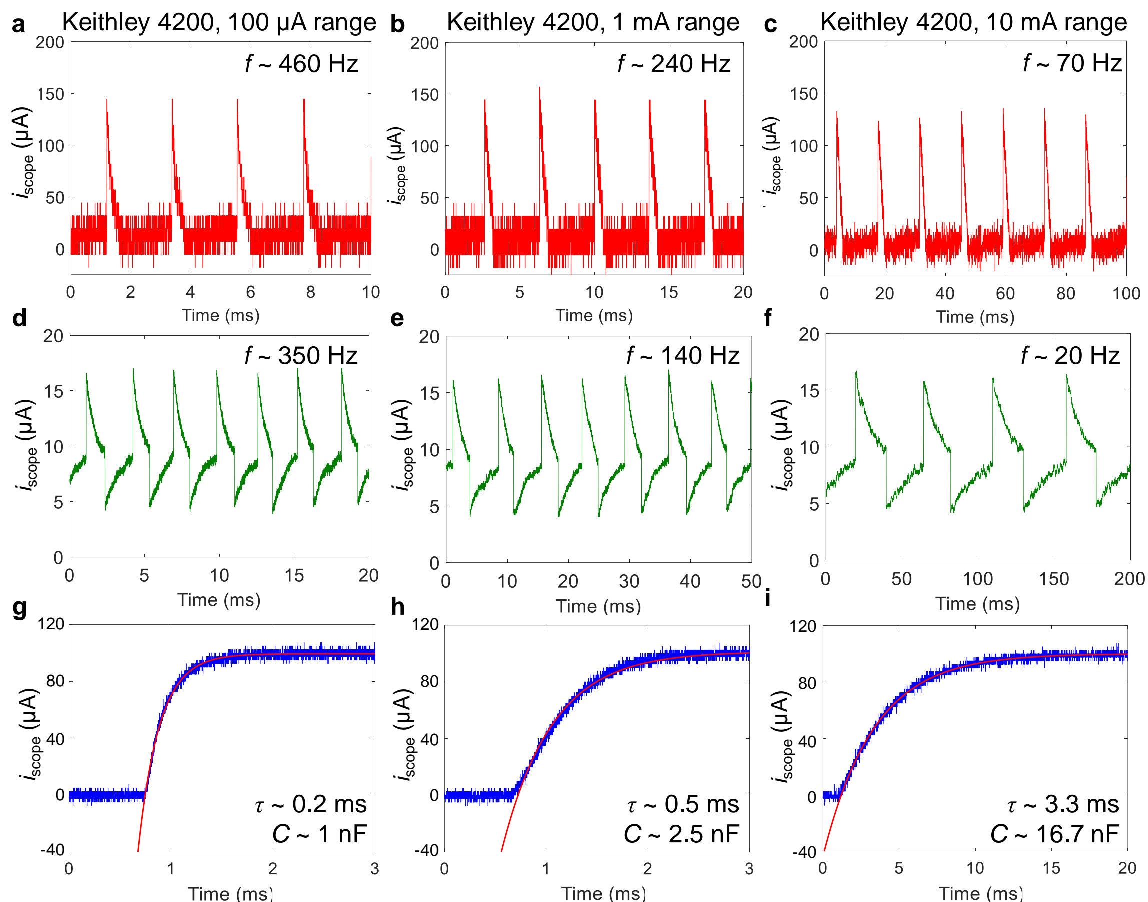

FIG. S7. Effect of a Keithley 4200-SCS current source's range settings on oscillation timescales. Oscillations of (a)-(c) a micrometer-scale VO_2 device ($L = 3.5$ µm, $W = 2.8$ µm) held at a fixed current bias of $I_S = 17$ µA, and (d)-(f) a nanogap device in IMT1 held at a fixed current bias of $I_S = 9$ µA applied using different current range settings. Note the very different timescales and frequencies (extracted from a Fast Fourier Transform). (g)-(i) Rise times measured by turning on a 100 µA current bias to a 200 kΩ resistor (with no device present). *RC* time constants were extracted from an exponential fit, and dividing by $R = 200$ kΩ yields an estimate for the capacitance present in the current source, cables, and probes.

In our experiments, we observe that the fast oscillations of continuous CNT heater devices [21] and of IMT2 in nanogap devices (Fig. S9) are insensitive to the choice of current source range. It may be that the oscillations are fast enough, or the resistance/voltage changes small enough, to be outside the response bandwidth of the current source feedback. Or it may be that the heating term modifies the dynamics such that the device preferentially oscillates independently, driven by its own smaller thermal and electrical time constants rather than being influenced or limited by external parasitics.

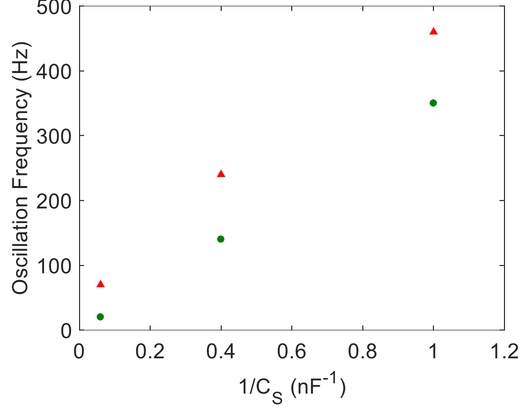

FIG. S8. Oscillation frequency of slow (sub-kHz) VO_2 devices without any CNT (red triangles) and nanogap devices in IMT1 (green circles) as a function of extracted effective source output capacitance (C_S), which varies with the current source range settings.

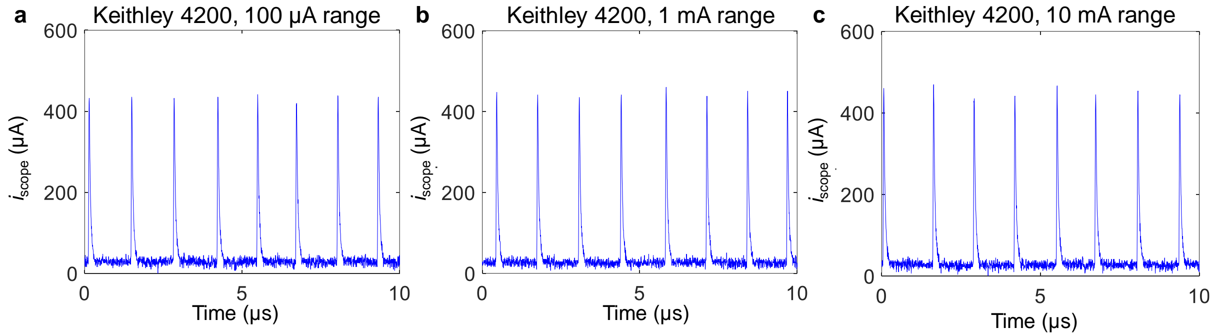

FIG. S9. Oscillations of a nanogap device held within its IMT2 at a fixed current bias I_S = 50 μA applied using different current range settings on a Keithley 4200-SCS. Unlike oscillations in IMT1, the source settings have no discernable impact on frequency in IMT2 (all are 0.7 MHz).

d. Impact of the Series Resistor (R_S) on Oscillations

A full set of oscillation measurements with different R_S are shown in Fig. S10 for a micrometer-scale VO_2 device (corresponding to Figs. 4a-4c in the main text). For all values of R_S from 200 kΩ to 1.5 MΩ, the VO_2 device without a CNT oscillates slowly at sub-kHz frequencies. The fast transient spike at the rising edge of each longer spike remains present in all oscillations but is not captured in Fig. S10. Different noise levels are a result of different modes used on the scope (e.g., high time-resolution mode; as well as different vertical resolutions), not intrinsic to the device dynamics. Lower bias currents were used at higher values of R_S as the oscillations occurred over a narrower range of currents. At higher values of R_S such as 2 MΩ, the device does not oscillate (or it does over such a small current range that it becomes effectively inaccessible).

In IMT2 of a VO_2 nanogap device, shown in Fig. S11 (corresponding to Fig. 4d-4f in the main text and Fig. S1a), oscillations are generally fast (sub-MHz) with R_S having no clear impact. At small R_S (200 kΩ or below), this device shows slow sub-kHz oscillations similar to the large VO_2 devices (the rising edge transient spike is also present but not displayed). This slowdown at smaller R_S is not a permanent change in the device behaviour, and likely represents an increased coupling to the large source capacitance.

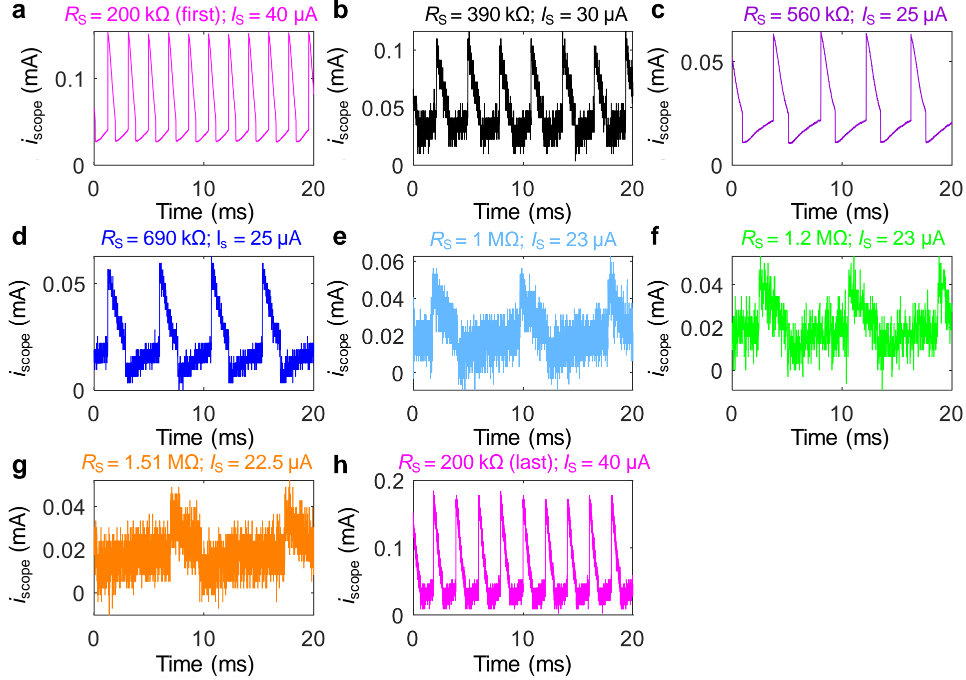

FIG. S10. Oscillations of a micrometer-sized VO_2 device ($L \sim 5$ μm, $W \sim 5$ μm) with different series resistor R_S and bias current I_S, as labelled. (a)-(g) Oscillations remain slow for all values of R_S tested. (h) The device did not permanently shift in oscillation frequency after these measurements.

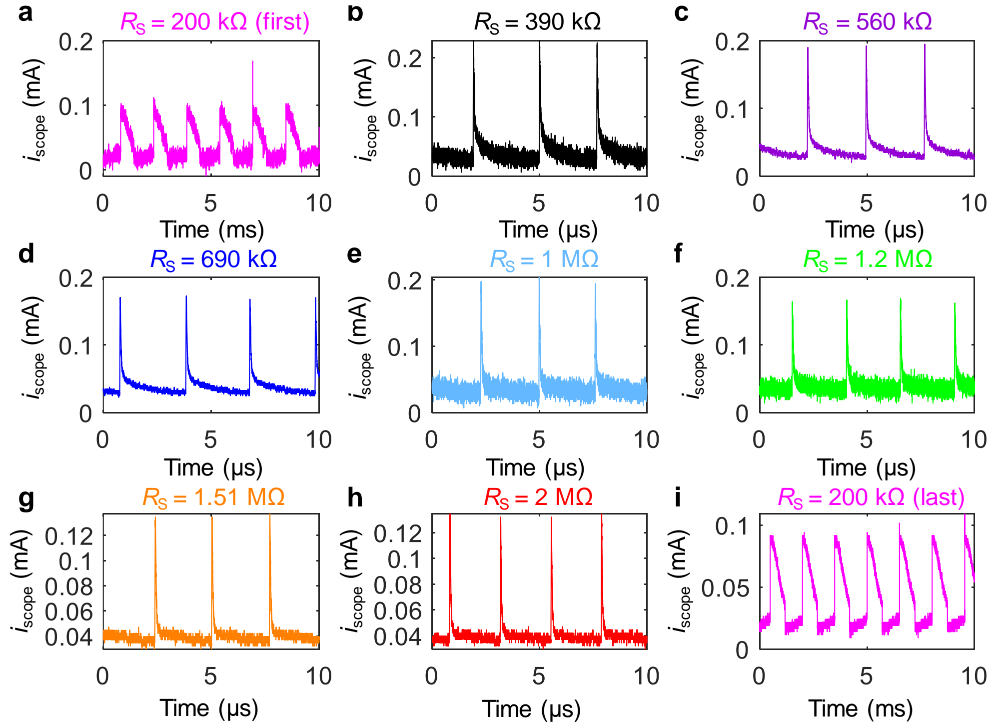

FIG. S11. Oscillations of a nanogap device in IMT2 (L = 4.7 μm) with different series resistors R_S, as labelled, with a fixed bias current of 40 μA. Oscillations are (a) slow for R_S = 200 kΩ and (b)-(h) fast for all larger values of R_S tested. To verify the device did not permanently change to exhibit fast oscillations, the measurement at 200 kΩ was repeated in (i) after all others.

e. Temperature Dependence

The switching voltages for both IMT1 and IMT2 decrease with increasing ambient temperature, as shown in Fig. S12 for the device in main text Fig. 1. This is consistent with a thermally-driven mechanism in which less power is required to heat the VO_2 to T_{IMT} if the device is held at a higher ambient temperature. At all temperatures, the ratio of V_{IMT1} to V_{IMT2} remains approximately 0.55.

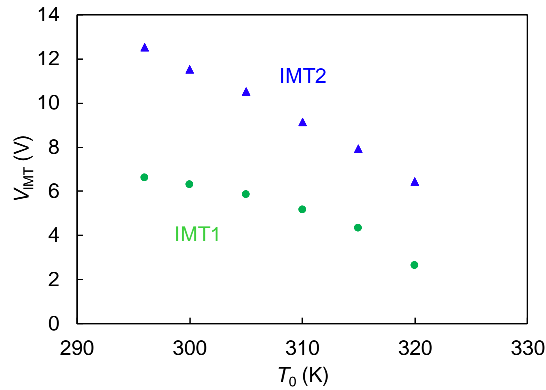

FIG. S12. Dependence of the DC switching voltage on ambient (stage) temperature, for both IMT1 in the gap (green circles) and IMT2 along the CNT (blue triangles). Both IMT voltages decrease with increasing ambient temperature.

f. Incubation Time and Switching Energy

A device's incubation time (switching delay) can be estimated by applying a voltage pulse and measuring the time taken to observe a jump in current at the IMT. Typically the incubation time decreases as the amplitude of the applied voltage pulse increases [8], and is associated with the time needed to heat the device to its IMT temperature (i.e., a thermal time constant), and/or with the time needed to charge capacitances (intrinsic or parasitic) and reach the switching voltage at the device terminals (i.e., an electrical time constant). The incubation times may give some insight into the switching speed of devices, but do not represent the same conditions used to generate oscillations, and do not capture the full dynamical behaviour.

Because our devices had higher switching voltages than most fast voltage pulse sources can supply (typically limited to 10 V amplitude), the pulsed units in a Keithley 4200-SCS parameter analyzer were used to generate higher voltage pulses up to 40 V. The rise and fall times of pulses were limited by the tool to 100 ns. In nanogap devices with a lower switching voltage, an Agilent 81150A pulse generator was used, which had a faster rise time. However, devices exhibited ringing below ~70 ns rise times, so the results with 100 ns rise times are shown in Fig. S13 for better comparison with other devices. The voltage across a 50 Ω oscilloscope in series with the device was used to measure the device's current waveform. Example waveforms for a VO_2 device without a CNT, a VO_2 device with a continuous (uncut) CNT heater, and a VO_2 nanogap device with a cut CNT are shown in Figs. S13a-S13c, respectively.

Figs. S13d-S13f shows extracted incubation times for these devices, with the left edge of each plot (lower limit of the horizontal axis) set as the static switching voltage for the device. The time for switching was taken as the start of the pulse (including rise time) to the start of the rising edge of the capacitive overshoot spike produced upon IMT. At high voltages, the extracted incubation time is thus limited by the rise time of the pulses (0.1 μs). The incubation times of all devices decrease with increasing pulse amplitude. However, note that the pulse voltage at the source is plotted, which is not the same as the voltage at the Pd contacts or at the nanogap (due to parasitics, contact resistance, and the series resistance of the long CNT electrodes). All three devices can achieve similar timescales for incubation, though the continuous CNT device is slightly slower because of its longer length. These timescales are generally considerably faster

than the delay times seen in slow (sub-kHz) spiking, which supports the postulate that the oscillation frequency is not limited by the device itself during this oscillation regime.

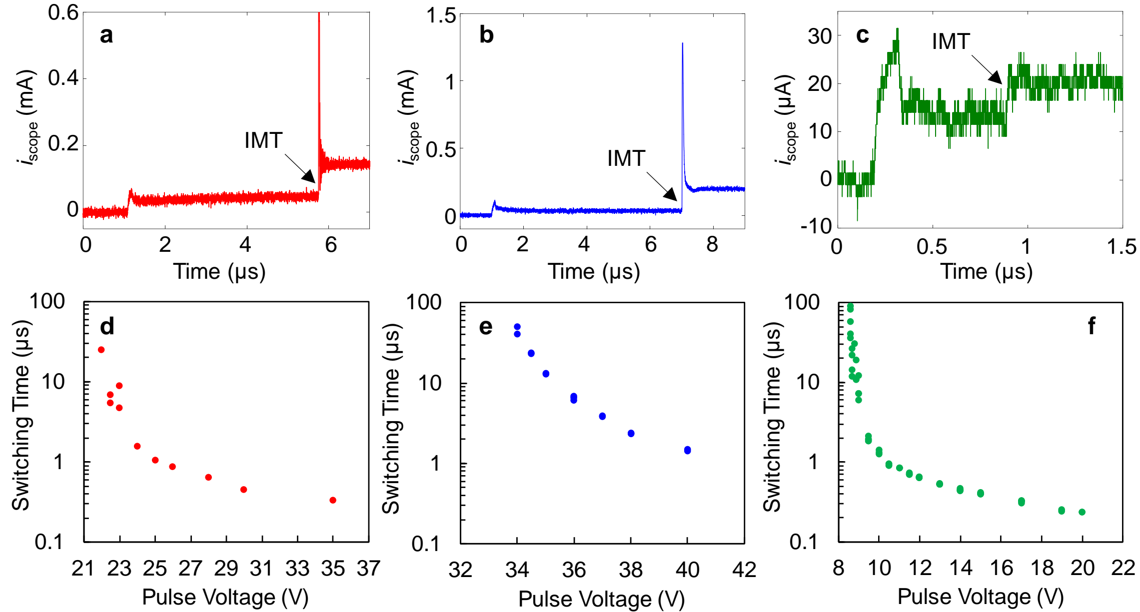

FIG. S13. Current waveforms when (a) a 23 V voltage pulse is applied to a VO_2 device without a CNT (L = 1 μm, W = 5 μm), (b) a 36 V voltage pulse is applied to a VO_2 device without a CNT (L = 7 μm, W = 6 μm), and (c) an 11.5 V voltage pulse is applied to a VO_2 gap device with CNT electrodes (L_{gap} < 100 nm, L = 3.4 μm, W = 6.3 μm). (d)-(f) Incubation times at different pulse amplitudes for the same devices.

Switching energy (Fig. S14) can be estimated by integrating device power over time using the measured waveforms. The voltage across the device terminals was not directly measured because the 1 MΩ input impedance of an oscilloscope in parallel with the device will disturb its operation if used to measure the device's voltage, given that the insulating state resistance of a VO_2 device is on the order of a few MΩ. Thus, the device voltage was approximated by subtracting the voltage drop across the series resistor from the input voltage pulse waveform (using $V_{device} \sim V_S - I_{device}(t)R_S$). In the presence of parasitic capacitors, the voltage seen by the device may be even lower, and thus the switching energy estimates presented here are upper bounds. While the VO_2 device without a CNT and the VO_2 device with a continuous CNT heater showed similar switching energies on the order of nJ, the nanogap device had a much lower switching energy down to 85 pJ. This is consistent with smaller thermal and switching volumes in the nanogap device.

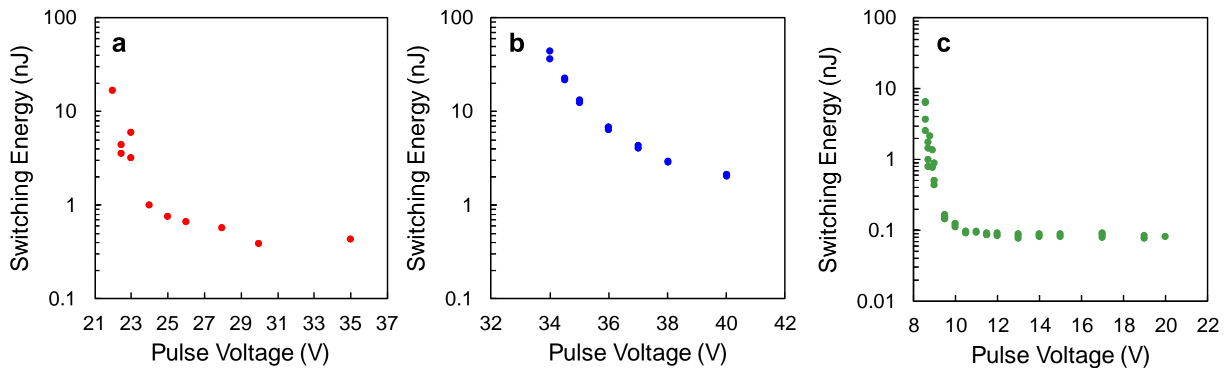

FIG. S14. Estimated upper bounds of switching energies for (a) a VO_2 device without a CNT (L = 1 μm, W = 5 μm), (b) a VO_2 device with a continuous CNT heater (L = 7 μm, W = 6 μm), and (c) a VO_2 nanogap device with CNT electrodes (L_{gap} < 100 nm, L = 3.4 μm, W = 6.3 μm).

3. Additional Scanning Probe Microscopy Measurements

a. Kelvin Probe Microscopy

Kelvin Probe Microscopy (KPM) was done in dual pass mode while a constant external voltage bias was applied to the device in Figs. S1a and S3a. One of the Pd electrodes was grounded, and the other was connected to the 200 kΩ series resistor to which the positive bias V_S was applied. These were outside the top and bottom of the scan area, respectively. During each scan, the device current remained steady and set in its insulating or metallic state. A full series of KPM images at different biases is shown in Fig. S15, after a first-order flattening operation was applied.

Before flattening, the surface potential along the device from grounded to positive electrode shows a nearly linear increase, corresponding to a constant electric field. However, because the VO_2 in the nanogap is more resistive than the CNT there is a higher field across it, corresponding to a sharper slope (Fig. S16a). Flattening removes the average slope of the potential and highlights any local changes in field across the device, namely within the nanogap. There is a much larger contrast observed in flattened images of the insulating state over the metallic state because of the larger deviation in field across the VO_2 in the gap relative to the metallic CNT, as shown in Fig. S16b.

Reversing the polarity or direction of applied bias reverses the field direction, and therefore inverts the contrast seen in the flattened image, but does not otherwise affect the surface potential profile or device operation (Fig. S17).

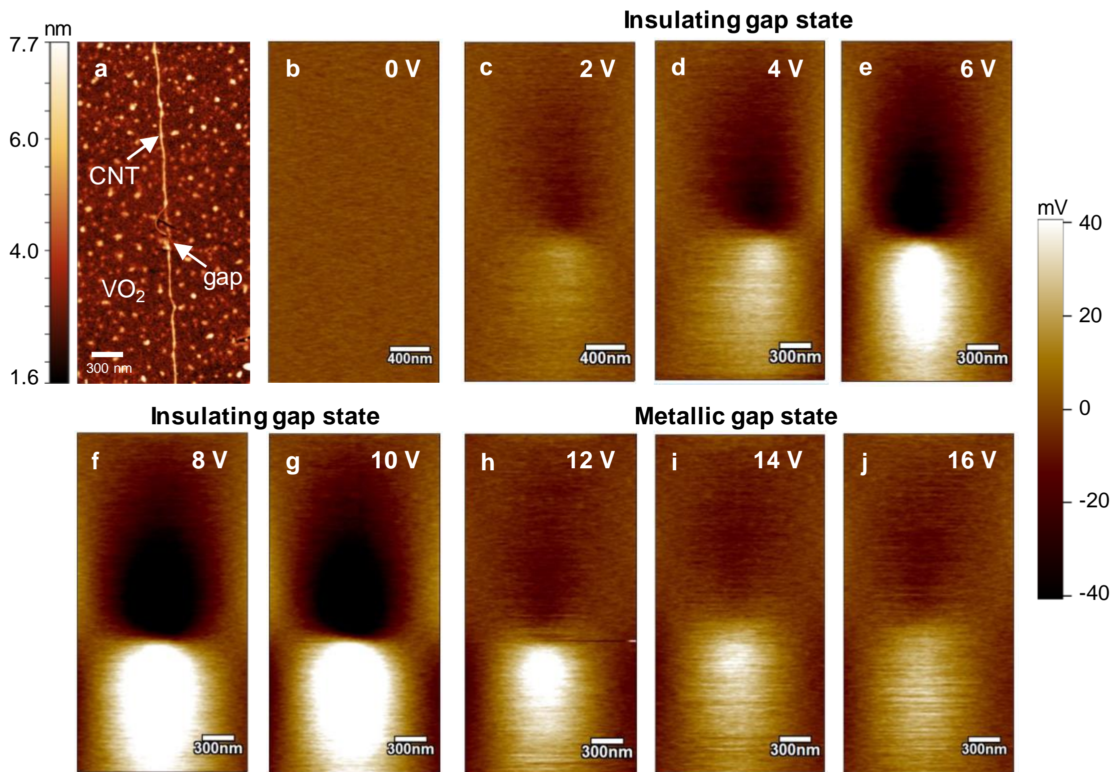

FIG. S15. Full set of KPM images of a nanogap device. (a) Topography of the cut CNT in a nanogap device, with an arrow indicating the gap location. (b) KPM of the same device and location with no device bias. (c)-(j) Flattened KPM images of the device with increasing bias. The Pd electrodes are outside the top and bottom margin of the images, with the bottom electrode biased positive. Images (c)-(g) are of the insulating VO_2 state in the nanogap, and (h)-(j) are of the metallic nanogap state. For better comparison, the same scalebar for surface potential is used in all images (some images are saturated).

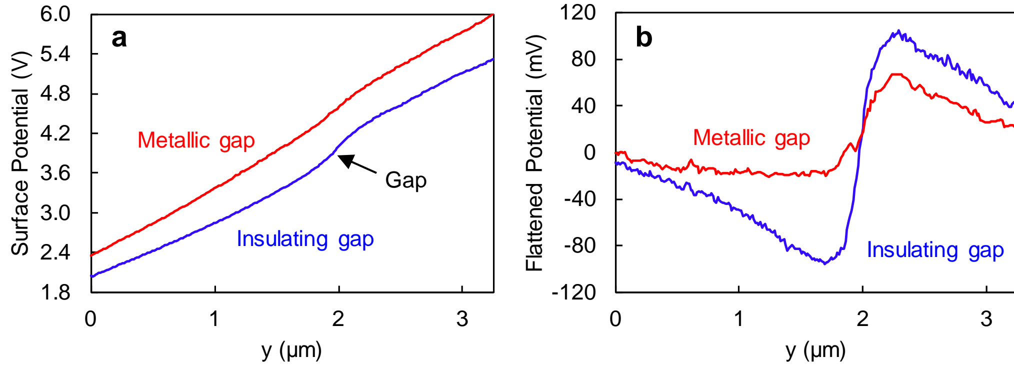

FIG. S16. (a) KPM surface potential profiles along the CNT prior to flattening, for a 10 V applied bias (blue) with an insulating gap state and 12 V applied bias (red) with a metallic gap state. (b) KPM surface potential profiles along the CNT after a first-order flattening operation effectively removes the average slope of each line in (a). These correspond to profiles along the vertical direction in Figs. S15g-S15h.

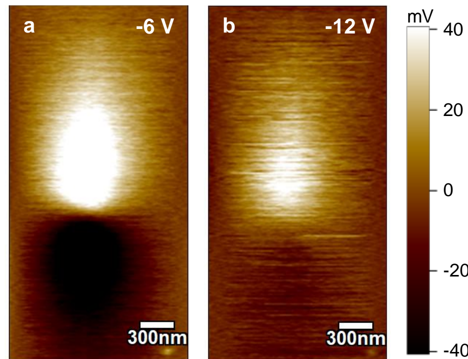

FIG. S17. KPM of the nanogap device in Fig. S15 with the bias polarity reversed (a negative bias is applied to the series resistor and contact beyond the bottom of the scan, and the contact outside the top of the scan is grounded), showing (a) the insulating gap state and (b) the metallic gap state.

b. Scanning Thermal Microscopy

Scanning thermal microscopy was performed in passive mode with a contact mode setpoint of 0.5 V and a 0.5 V tip bias. The SThM tip is made of Pd on SiN (model PR-EX-GLA-5 from Anasys®), with a tip radius of <100 nm, that senses changes in device heating via a change in tip resistance. The tip requires electrical isolation from the biased device, and thus devices were capped with a 35 nm layer of 2% 495K poly(methyl methacrylate) (PMMA) in anisole. The PMMA was spin coated at 7000 rpm for 40 s, followed by baking on a hotplate at 180°C for 5 min. A PMMA layer was used because oxide deposition can reduce the stability of the CNT and VO_2. All scans were taken on the surface of this PMMA layer, and thus the thermal profile observed is expected to be broader than that of the VO_2 surface.

A set of SThM images at multiple V_S bias points is shown in Fig. S18. The same nanogap device was used as for the KPM measurements, corresponding to Figs. S1a and S3a. A 200kΩ series resistor was used for all measurements. Because V_S = 10 V was very close to IMT1, and the threshold voltage was prone to shifting very slightly over time and cycles, this bias point corresponds to the insulating state in KPM but the metallic state in SThM.

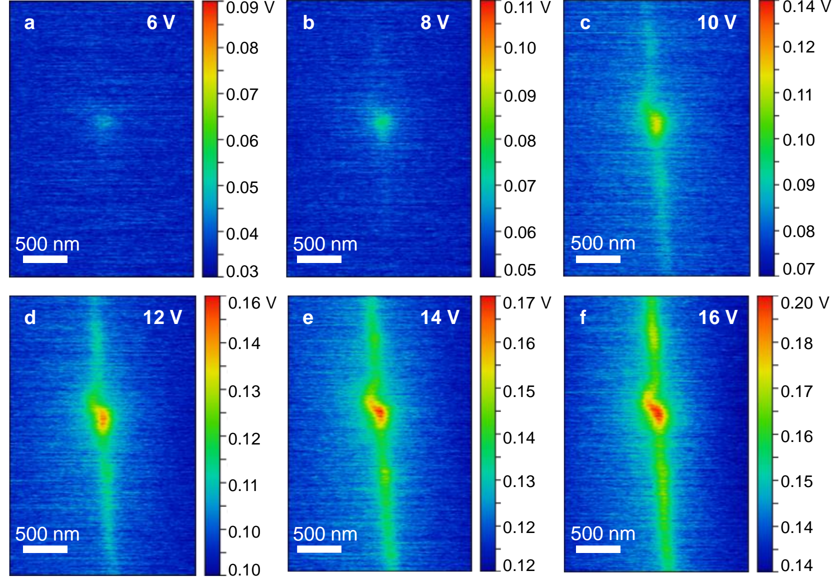

FIG. S18. SThM images showing heating profiles of a nanogap device at different device biases, as seen on the surface of a 35 nm PMMA capping layer. (a)-(b) When the VO_2 within the CNT nanogap is insulating, heating is highly localized to the gap. (c)-(f) After IMT1, the VO_2 in the gap is metallic and the CNT is connected, causing heating along its length.

4. Finite Element Modeling

We constructed a 3D electrothermal finite element model for nanogap devices using COMSOL Multiphysics. This self-consistently coupled together calculations for the voltage (V) and current density (J) in the device (Eqn. (S1), which depends on temperature T through the electrical conductivity σ) with calculations for the temperature (Eqn. (S2), which is affected by Joule heating).

$$\nabla \cdot (\sigma(x, y, z, T)\nabla V) = 0 \tag{S1}$$

$$\nabla \cdot (k\nabla T) + J \cdot E = 0 \tag{S2}$$

E is the electric field in the device, and k is the thermal conductivity of VO_2. For the VO_2, the electrical conductivity was scaled with local temperature based on resistance measurements of VO_2 devices without a CNT as a function of ambient temperature. At room temperature, a σ(296 K) = 80 S/m was estimated after subtracting contact resistance, and was scaled according to experimental temperature dependence to produce a $\sigma(T)$ function. A nearest-neighbour interpolation of the function was used (with steps of ~1 K), which rounds the temperature of an element to the nearest experimental data point and uses the corresponding resistance. These discrete steps are necessary to avoid convergence issues. If a smooth curve or a linear interpolation is used within the IMT region (which is highly nonlinear) then a slight change in temperature can cause a large change in resistance from one solver step to the next, making convergence difficult.

The conductivity of the CNT is given by [37]:

$$\sigma_{\mathrm{CNT}}(T, V, L) = \frac{4q^2}{h}\frac{\lambda_{\mathrm{eff}}}{A} \tag{S3}$$

$$\text{where } \lambda_{\mathrm{eff}} = \left(\lambda_{\mathrm{AC}}^{-1} + \lambda_{\mathrm{OP,ems}}^{-1} + \lambda_{\mathrm{OP,abs}}^{-1} + \lambda_{\mathrm{defect}}^{-1}\right)^{-1} \tag{S4}$$

λ_{eff} is an effective electron mean free path (MFP) that combines contributions from elastic electron scattering with acoustic phonons (λ_{AC}), as well as inelastic electron scattering by optical phonon absorption ($\lambda_{OP,abs}$) and emission ($\lambda_{OP,ems}$). Emission is influenced by the electric field, so this term is dependent on the voltage and CNT length, and all MFPs are a function of temperature. Values of $\lambda_{OP,300}$ = 20 nm and $\hbar\omega_{OP}$ = 0.2 eV are used here. An additional scattering term for defects (λ_{defect}), with a mean free path of 1 µm, is added to better represent *I-V* characteristics of our imperfect CNTs. For additional details, see Refs. [21,37].

The geometry of the simulated devices is shown in Fig. S19. For simulations shown in main text Fig. 2 the actual experimental CNT shape and location were extracted from AFM images (Fig. S1a) and used in the simulation (including a lateral offset in the width, and the curvature of the CNT end). For these simulations only, a 35 nm capping layer made of PMMA was included. For all other simulations, the CNT was centered in the width of the device and only half the device width was simulated due to symmetry. The nanogap was centered at *L*/2 and its length was varied. The simulated TiO_2 substrate was 2 µm thick (unlike the ~500 µm experimental TiO_2), which was sufficient to capture its thermal resistance. The electrical and thermal conductivities used for the various materials are listed in Table 1.

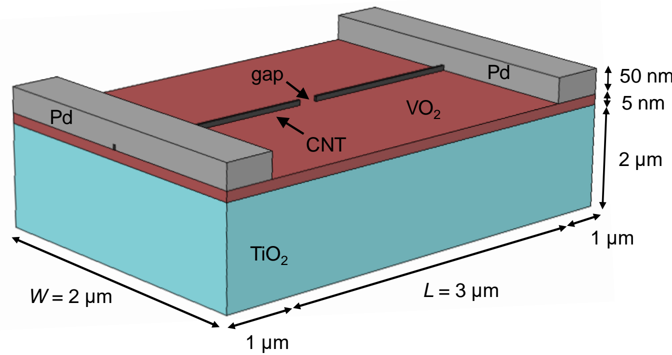

FIG. S19. The structure used to simulate the nanogap devices with an electrothermal finite element model. Only half the width was simulated due to symmetry. For simulations in main text Fig. 3, experimental CNT and VO_2 dimensions were used, with *L* = 5 µm and *W* = 5 µm (the full width was simulated).

The top of one Pd electrode was held at a fixed voltage, and the other grounded. An electrical contact resistance was included for various interfaces: CNT/Pd (25 kΩ), CNT/VO_2 (~100 kΩ), and VO_2/Pd. The VO_2/Pd interface resistivity was set to 1×10^{-3} Ω·cm^2 and reduced with increasing local temperature, in the same manner as the VO_2 electrical resistivity. When simulating a voltage sweep, the solution for the previous voltage point was used as the initial conditions for the next voltage.

The bottom of the TiO_2 was set to room temperature (296 K), and all other boundaries to thermally insulating. A thermal boundary resistance was included for various interfaces: TiO_2/VO_2 (1×10^{-8} m^{2}K/W), VO_2/CNT (5×10^{-9} m^{2}K/W), VO_2/Pd (1×10^{-8} m^{2}K/W), CNT/Pd (1×10^{-8} m^{2}K/W), and PMMA/VO_2 (1×10^{-8} m^{2}K/W). Experimental values for these particular interfaces have not been measured, so average values within typical ranges were used [38].

Table 1. Material properties used in simulations

	σ [S/m]	**k [Wm^{-1}K^{-1}]**
TiO_2	10^{-7}	7
VO_2	*T*(*x*,*y*,*z*) spanning 80 to 2×10^6	3
CNT	Eqns. S3, S4	600
Pd	10×10^6	72
PMMA	10^{-10}	0.1

The model used a segregated approach, solving first for temperatures and then for electric fields. Each step used the direct PARDISO solver (as opposed to an iterative solver). A damping factor of 0.2 was used in the temperature step, and 0.8 in the electric field step. Reducing the damping factor results in a lower change between solver steps and aids in convergence, by avoiding overshoots across the IMT and MIT (especially in temperature).

Simulated voltage sweeps (with increasing voltage only) are shown in Fig. S20a for different nanogap sizes. The IMT1 voltage (V_{IMT1}) scales approximately linearly with gap size, as shown in Fig. S20b, and corresponds to switching of the VO_2 between the cut CNT ends (and a small volume just underneath the CNT ends, as the VO_2/CNT contact resistance generates heat). A second IMT event (IMT2) occurs when VO_2 along the entire length of the CNT is heated to its transition temperature. The IMT2 switching voltage at V_{device} ~ 9 V is nearly the same as for a simulated device with a continuous CNT. Because the IMT2 voltage does not significantly vary with gap size but V_{IMT1} does, the ratio V_{IMT1}/V_{IMT2} increases with increasing gap size. If the gap size is sufficiently large (here >100 nm), then only a single IMT event occurs, at a voltage between that of a VO_2 device with a continuous CNT and a VO_2 device with no CNT.

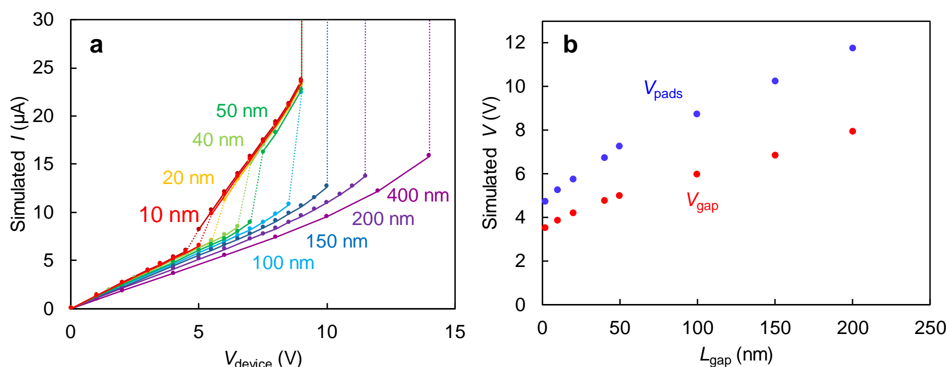

FIG. S20. (a) Simulated *I-V* characteristics for different nanogap lengths (L_{gap}) in the CNT, with fixed Pd contact spacing L = 3 μm. Increasing the gap size results in a higher IMT1 switching voltage and a large change in current across the IMT, but a similar IMT2 voltage. (b) IMT1 switching voltage at the Pd contacts (blue, $V_{IMT1} = V_{pads}$) and as seen at the ends of the CNT (at the contacts to the gap, in red, V_{gap}) with the series resistance of the CNT and the Pd contact resistance subtracted.

Fig. S21 shows the dependence of simulated IMT1 and IMT2 switching voltages on ambient temperature for a 50 nm gap length (with L = 3 μm). The results match the trends in Fig. S12, which are consistent with a thermally-triggered IMT. The V_{IMT1}/V_{IMT2} ratio is higher in simulations than experiment. In real devices the CNT quality and contacts may be worse, leading to a higher V_{IMT2}.

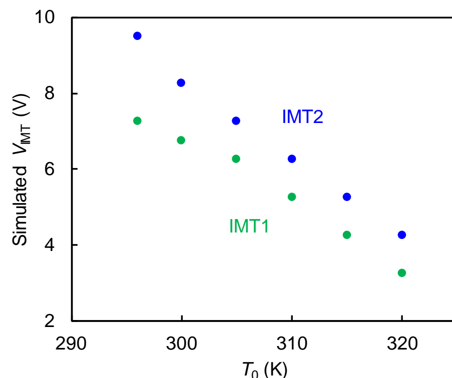

FIG. S21. The switching voltage of both IMT events decreases with increasing ambient temperature in a device with a 50 nm CNT gap, similar to experiment in Fig. S12.

5. Compact Modeling in LT Spice

To examine the role of various electrical and thermal parameters on the oscillation frequency of resistive switching devices, we constructed a compact model using LT Spice. For an explanation of relaxation oscillators and how oscillations can be produced, please see the Supplemental Material of [19].

In this model, the device current i_m was controlled by nonlinear thermally-activated Schottky transport, given by:

$$i_m = AT^2 \exp\left(\frac{(\beta\sqrt{V_m/d} - \phi)}{k_B T}\right) \quad \text{(S5)}$$

v_m is the voltage across the device, A is a constant (the device cross-sectional area multiplied by the Richardson constant), and d its length. ϕ is an energy barrier, k_B is the Boltzmann constant, and β is a constant that depends on the dielectric constant [30]. T represents an average device temperature set by the thermal dynamics, which are approximated using Newton's law of cooling, as described in the main text:

$$C_{th}\frac{dT}{dt} = i_m v_m + \frac{v_m^2}{R_{heater}} - \frac{T - T_0}{R_{th}} \quad \text{(S6)}$$

T_0 is the ambient temperature, C_{th} is the thermal capacitance of the device (which scales with the switching volume heated and cooled across the transition), and R_{th} is a thermal resistance associated with the efficiency of heat transport out of the switching volume. T, R_{th}, and C_{th} are lumped values used to emulate the device's dynamics and are coarse approximations to physical values, which in reality vary spatially (especially across a narrow metallic conduction region) and with temperature. We do this to generate a compact model which is fast to run and easily integrable into larger circuits (i.e. with multiple oscillators), unlike finite element models, in which the transient simulations have too many degrees of freedom to accomplish this (especially in devices with a CNT). R_{heater} (if any) is a resistive heater electrically in parallel with the device, which contributes to an increase in device temperature by Joule heating.

The device M was integrated into a circuit with several additional resistances and capacitances, shown in Fig. S22a. These include the external series resistor R_S and the oscilloscope, which has an input impedance of 50 Ω, placed in series with the device. Several resistances and capacitances representing device contact resistance and parasitic capacitance (both from the source and the device) were also included. The circuit was solved simultaneously and self-consistently with Eqns. (S5) and (S6) in LT Spice. C_{th} was varied between 1×10^{-14} J/K to 5×10^{-17} J/K, and if included, R_{heater} was varied between 400 kΩ and 3 MΩ. Values of other parameters are listed in Table 2. An alternative circuit [19] is shown in Fig. S22b, with both parasitic capacitances placed effectively within the device rather than having the large dominant capacitor in the current source. We see similar results with this configuration, such that a modification to the thermal dynamics (i.e. a small C_{th} in combination with a heat source) can produce faster oscillations regardless of the large capacitor's exact location, avoiding its excitation. Thus, even if oscillation frequency is expected to be limited by a parasitic device capacitance, it may be possible to avoid its excitation through careful device and measurement circuit design. Similarly, if a device or network of devices contains multiple capacitances it may be possible to access several different oscillatory time scales.

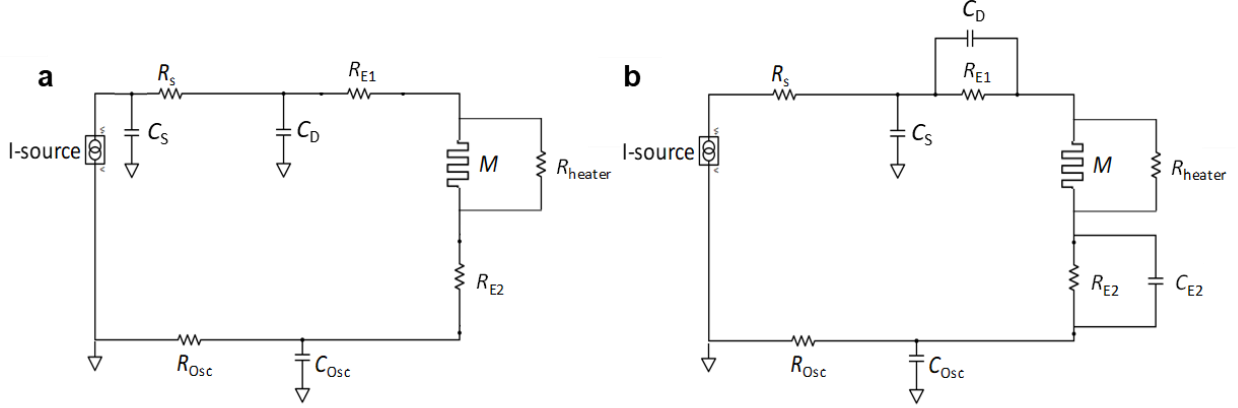

FIG. S22. Circuit schematic used for simulations in LT Spice. The circuit consists of a switching device *M* in parallel with a thermally coupled resistive heater R_{heater} (such as a CNT), an external current source, an external series resistor R_S, an oscilloscope in series represented by R_{osc} and C_{osc}, and additional parasitics and device resistances and capacitances. E1 and E2 refer to the two electrodes of a planar device. (a) The model used in main text Figs. 5 and 6, and (b) an alternative model with both capacitors associated with the device.

Table 2. Parameters used in SPICE Simulations

Parameter	Value, Main Model	Value, Alternative
T_0	296 K	296 K
β	3.3×10^{-4} eV · m$^{1/2}$	3.3×10^{-4} eV · m$^{1/2}$
A	1.7×10^{-9} A · K^{-2}	1.7×10^{-9} A · K^{-2}
D	5 μm	5 μm
R_{th}	2.5×10^{8} K · W^{-1}	2.5×10^{8} K · W^{-1}
C_S	5 nF	5.5 nF
C_D	30 pF	15 pF
R_{E1}	10 $k\Omega$	27 $k\Omega$
C_{E2}	–	0.5 fF
R_{E2}	10 $k\Omega$	1 $k\Omega$
R_S	varied, 100 $k\Omega$	300 $k\Omega$
ϕ	0.58 eV	0.58 eV
R_{osc}	50 Ω	50 Ω
C_{osc}	100 pF	100 pF
k_B	8.62×10^{-5} eV · K^{-1}	8.62×10^{-5} eV · K^{-1}
I_S	$3 - 5\ \mu$A	6 μA

These models produce abrupt resistive switching during a DC voltage sweep, with a change in device current by several orders of magnitude across the transition, displayed in Fig. S23a for the model in Fig. S22b (both models produce similar DC behaviour as only the capacitors are significantly different). This is caused by an electrothermal runaway process due to feedback, and although not physically an IMT it produces similar electrical behavior. Similar behavior can also be achieved with other nonlinear thermally-activated transport such as Poole-Frenkel [30], and can also lead to oscillations. When a DC current sweep is performed (Fig. S23b), the positive temperature-current feedback is restricted, and the device produces negative differential resistance (NDR) behavior with accompanying oscillations. When a 600 kΩ heater is

included (Figs. S23c-S23d), the switching voltage is reduced and the insulating state current is higher (as the heater provides a parallel conductive path for current to flow), reducing the on/off ratio (the metallic state is limited by the series resistance). Both devices show NDR during a current sweep and oscillate. Hysteresis was not included, for ease of calculations. To study periodic oscillations, the circuit was biased with a constant current source, $I_S \sim 5$ μA, which operates the device within its region of NDR.

As the tuning parameters C_{th} and G_{heater} ($1/R_{heater}$) are varied these systems can abruptly change between slow ~kHz oscillations and faster ~MHz oscillations, as discussed in the main text. Fig. S24 maps oscillation frequency as a function of these tuning parameters for the configuration in Fig. S22b (a cross section of this plot along fixed R_{heater} produces a plot similar to main text Fig. 5e). When there is no heater present, or a very resistive heater that does not produce significant heating (zero or small G_{heater}), a reduction in C_{th} (representing the thermal switching volume, which is reduced as the device is scaled) appears unable to produce faster oscillations. However, if both C_{th} and R_{heater} are sufficiently small, then fast oscillations occur, demonstrating that adding a heater in addition to scaling the device is one way to speed up the system.

We note that self-sustained oscillations did not occur when a very small resistor R_{heater} is used, which prevents effective access of the NDR in the VO_2 by electrically shorting it. Fast oscillations also did not occur when a parallel resistor was electrically included in the circuit but which did not contribute to heating (i.e., no term involving R_{heater} added to Eqn. S6).

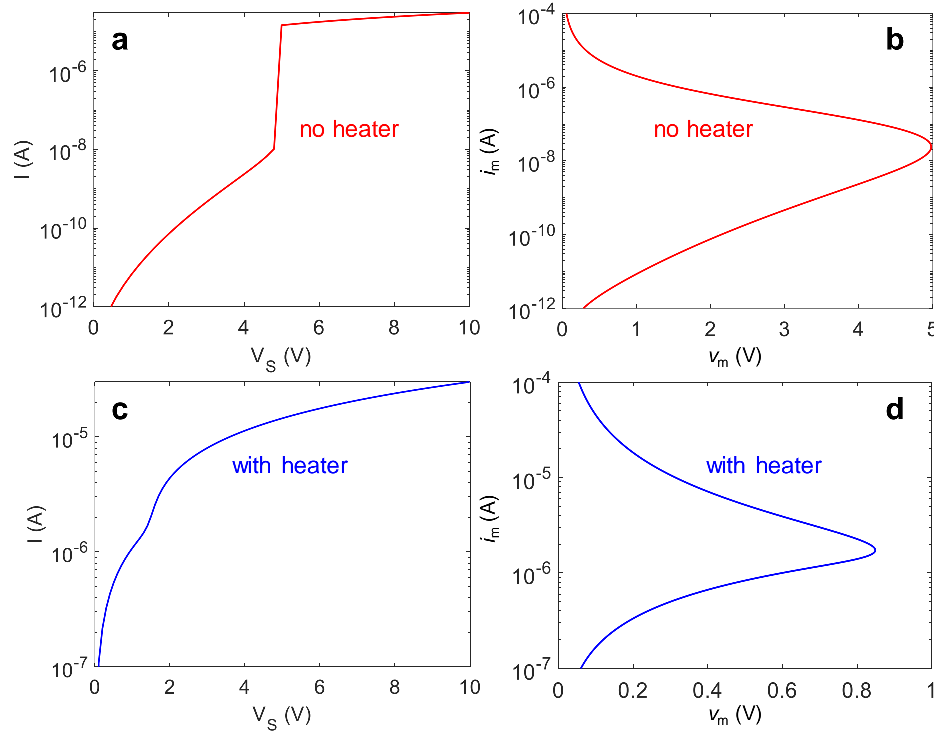

FIG. S23. DC *I-V* characteristics simulated in SPICE: (a) with a voltage source and no heater present, (b) with a current source and no heater, (c) with a voltage source and $R_{heater} = 600$ kΩ, and (d) with a current source and $R_{heater} = 600$ kΩ. Voltage sweeps are plotted as viewed from the source node (V_S), and current sweeps as seen at the device (v_m).

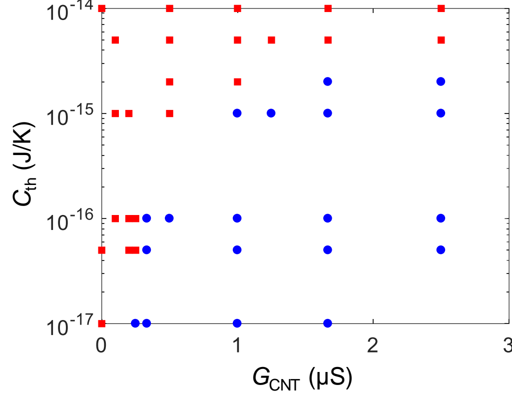

FIG. S24. Simulated oscillation frequency abruptly transitions between "slow" (red squares, ~kHz) and "fast" (blue circles, ~MHz) depending on the choice of C_{th} and heater conductance G_{heater} ($1/R_{heater}$).

Finally, using our model, we investigate whether slow parasitic oscillations or fast intrinsic oscillations occur for non-heater devices with different switching currents and resistances. The resistance in both the insulating and the metallic state may affect the electrical RC time scales within the circuit (though because resistance is continuously changing, a single fixed time constant(s) is insufficient to describe the full device dynamics).

In the electro-thermal device model, switching current is primarily adjusted by changing R_{th}, as a device that loses more heat to its surroundings will require a higher input current to reach the transition temperature. Fig. S25a shows simulated DC switching without R_S for several devices with different switching currents. To maintain a fixed switching voltage for each curve we have adjusted the activation energy ϕ. Oscillatory behaviour of these devices as thermal capacitance C_{th} and external series resistance R_S are varied are shown in Fig. S25b and Fig. S25c, respectively. These devices show similar behaviour, accessing fast intrinsic oscillations at high R_S and slow source-dominated oscillations at low R_S. However, the crossover value of R_S appears to change with the insulating state resistance.

We also simulate switching for several devices with a fixed insulating state resistance but different metallic state resistances, adjusted via R_{E1} and R_{E2}. DC switching without R_S for these devices is shown in Fig. 25Sd. We then simulate device oscillations including different values of R_S. If the metallic state resistance is very large, then fast oscillations can be accessed at a lower value of R_S (Fig. S25f). Thus, the lower insulating and metallic state resistance of the CNT heater devices may in part make it easier to access intrinsic oscillations by requiring a lower R_S.

These do not represent all possible combinations of switching characteristics, but the results do highlight that dynamical behaviour can depend to some degree on the electrical characteristics of the device in either its insulating or metallic state. In all these scenarios we still obtain fast intrinsic oscillations at high R_S and slow oscillations at low R_S.

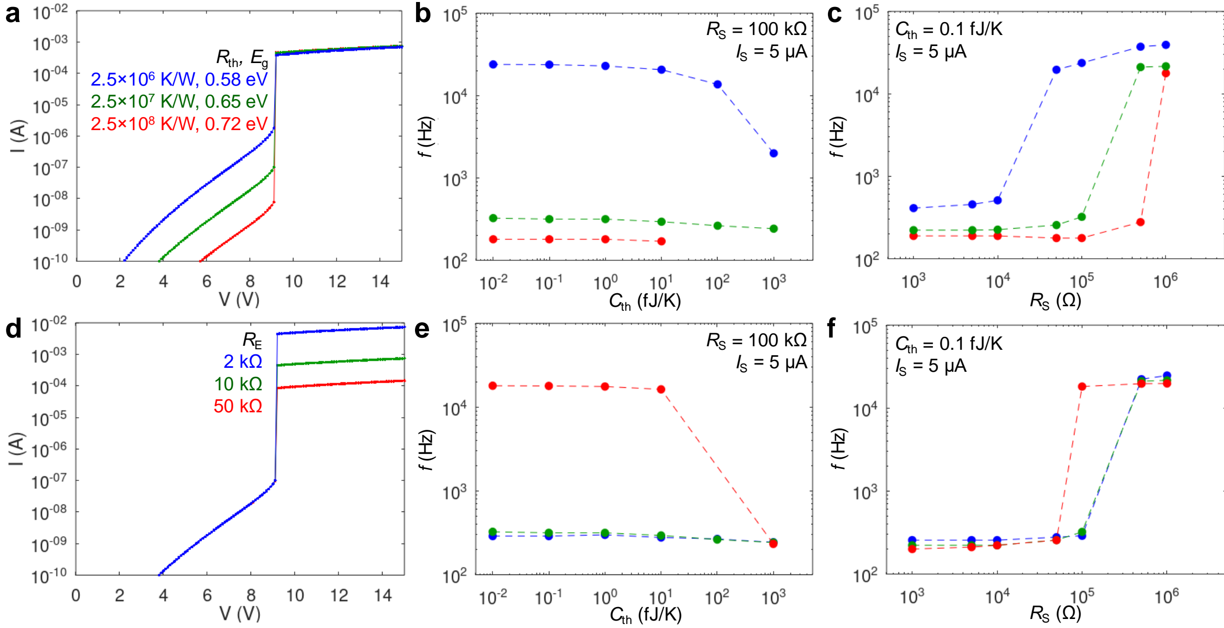

FIG. S25. Simulated effects of device resistance on accessibility of fast intrinsic oscillations. Voltage-controlled DC *I-V* characteristics are simulated in SPICE to produce (a) devices with different switching currents, with corresponding oscillation frequencies shown in (b) for different device thermal capacitance and (c) different external series resistance. Similar plots are shown in (e) and (f) for simulated devices in (d) with different metallic state resistance and therefore on/off ratio. Dashed lines are guides for the eye.

6. Video

Video S1 (provided as a separate file) shows the simulated steady state evolution of the electric field and temperature in a nanogap device ($L = 5$ μm, $W = 5$ μm) as the applied voltage is increased (see also Figs. 2c and 2f in the main text). The device dimensions correspond to that of the real device in Fig. S1a, which was also used for KPM and SThM measurements. The temperature shown is on the surface of the 35 nm PMMA capping layer, to best compare with SThM, but the VO_2 surface temperature is slightly hotter. IMT1 occurs between 10 - 11 V (the VO_2 in the gap is insulating for applied voltages $V_S \leq 10$ V and metallic for $V_S \geq 11$ V), and IMT2 occurs beyond 16 V in the simulation.

7. LT SPICE files

LT SPICE files which include the simulated circuit and compact device model, as well as all parameters, are included as additional supplemental files. These simulations were run in version 4.13m of LT SPICE.

References

[22] J. Jeong, N. Aetukuri, T. Graf, T. D. Schladt, M. G. Samant, and S. S. Parkin, Suppression of metal-insulator transition in VO_2 by electric field-induced oxygen vacancy formation, Science **339**, 1402 (2013).

[21] S. M. Bohaichuk, M. Muñoz Rojo, G. Pitner, C. J. McClellan, F. Lian, J. Li, J. Jeong, M. G. Samant, S. S. P. Parkin, H.-S. P. Wong, and E. Pop, Localized Triggering of the Insulator-Metal Transition in VO_2 Using a Single Carbon Nanotube, ACS Nano **13**, 11070 (2019).

[20] N. Patil, A. Lin, E. R. Myers, R. Koungmin, A. Badmaev, Z. Chongwu, H. S. P. Wong, and S. Mitra, Wafer-Scale Growth and Transfer of Aligned Single-Walled Carbon Nanotubes, IEEE Trans. Nanotechnol. **8**, 498 (2009).
[17] F. Xiong, A. D. Liao, D. Estrada, and E. Pop, Low-Power Switching of Phase-Change Materials with Carbon Nanotube Electrodes, Science **332**, 568 (2011).
[35] A. Liao, R. Alizadegan, Z.-Y. Ong, S. Dutta, F. Xiong, K. J. Hsia, and E. Pop, Thermal dissipation and variability in electrical breakdown of carbon nanotube devices, Phys. Rev. B **82** (2010).
[36] P. Avouris, T. Hertel, and R. Martel, Atomic force microscope tip-induced local oxidation of silicon: kinetics, mechanism, and nanofabrication, Appl. Phys. Lett. **71**, 285 (1997).
[24] H. J. Wan, P. Zhou, L. Ye, Y. Y. Lin, T. A. Tang, H. M. Wu, and M. H. Chi, In Situ Observation of Compliance-Current Overshoot and Its Effect on Resistive Switching, IEEE Electron Device Lett. **31**, 246 (2010).
[8] D. Li, A. A. Sharma, D. K. Gala, N. Shukla, H. Paik, S. Datta, D. G. Schlom, J. A. Bain, and M. Skowronski, Joule Heating-Induced Metal-Insulator Transition in Epitaxial VO_2/TiO_2 Devices, ACS Appl. Mater. Interfaces **8**, 12908 (2016).
[37] E. Pop, D. A. Mann, K. E. Goodson, and H. Dai, Electrical and thermal transport in metallic single-wall carbon nanotubes on insulating substrates, J. Appl. Phys. **101**, 093710 (2007).
[38] E. Pop, Energy dissipation and transport in nanoscale devices, Nano Res. **3**, 147 (2010).
[19] S. M. Bohaichuk, S. Kumar, G. Pitner, C. J. McClellan, J. Jeong, M. G. Samant, H.-S. P. Wong, S. S. P. Parkin, R. S. Williams, and E. Pop, Fast Spiking of a Mott VO_2-Carbon Nanotube Composite Device, Nano Lett. **19**, 6751 (2019).
[30] G. A. Gibson, Designing Negative Differential Resistance Devices Based on Self-Heating, Adv. Funct. Mater. **28**, 1704175 (2018).